J Mater Sci (2008) 43:6799–6833
DOI 10.1007/s10853-008-2966-6

REVIEW

Development of lanthanum strontium manganite perovskite cathode materials of solid oxide fuel cells: a review

San Ping Jiang

Received: 6 December 2007 / Accepted: 21 August 2008 / Published online: 18 October 2008

Abstract The high-temperature solid oxide fuel cell (SOFC) is the most efficient and environmentally friendly energy conversion technology to generate electricity from fuels such as hydrogen and natural gas as compared to the traditional thermal power generation plants. In the last 20–30 years, there has been significant progress in the materials development and stack technologies in SOFC. Among the electrode materials, lanthanum strontium manganite (LSM) perovskites, till today, are the most investigated and probably the most important electrode materials in SOFCs. The objective of this article is to review and update the development, understanding, and achievements of the LSM-based materials in SOFC. The structure, nonstoichiometry, defect model, and in particular the relation between the microstructure, their properties (electrical, thermal, mechanical, chemical, and interfacial), and electrochemical performance and performance stability are critically reviewed. Finally, challenges and prospects of LSM-based materials as cathodes for intermediate and low-temperature SOFCs are discussed.

Introduction

Recent worldwide interest in developing a hydrogen-based economy and in reducing the environmental pollution has focused attention on fuel cell technology and in particular the solid oxide fuel cells (SOFCs). SOFCs, being an electrochemical energy conversion device, have unique advantages over the conventional power generation technologies. They offer extremely high chemical-to-electrical conversion efficiencies because the efficiency is not limited by the Carnot cycle of a heat engine. Further energy efficiency can be achieved when the produced heat is used in combined heat and power, or gas turbine applications. Furthermore, the greenhouse gas emission from SOFC is much lower than that from conventional power generation technologies. Due to its high operating temperature, SOFC has a high tolerance to typical catalyst poisons, produces high-quality heat for reforming of hydrocarbons, and offers the possibility of direct utilization of hydrocarbon fuels.

A basic SOFC consists of an anode, an electrolyte, and a cathode (see Fig. 1). Driving by the differences in oxygen chemical potential between fuel and air compartments of the cell, oxygen ions migrate through the electrolyte to the anode where they are consumed by oxidation of fuels such as hydrogen, methane, and hydrocarbons (C_nH_{2n+2}). Thus, the electrolyte must be dense to separate the air and fuel, must possess high oxygen ionic conductivity but negligible electronic conductivity, and must be chemically and structurally stable over a wide range of partial pressure of oxygen and temperatures [1]. On the other hand, the anode must be porous, electrocatalytically active for the fuel oxidation reaction and chemically and thermally compatible with the electrolyte and interconnect. In the case of hydrocarbon fuels, anode must also possess certain tolerance toward sulfur and carbon deposition under SOFC operating conditions. Issues facing the development of anode materials of SOFC have been reviewed recently [2, 3].

The cathode is the material where pure oxygen or oxygen from air, combining electrons externally from the cell, is reduced to oxygen ions through the following electrochemical reaction.

S. P. Jiang (✉)
School of Mechanical and Aerospace Engineering, Nanyang Technological University, Singapore 639798, Singapore
e-mail: mspjiang@ntu.edu.sg

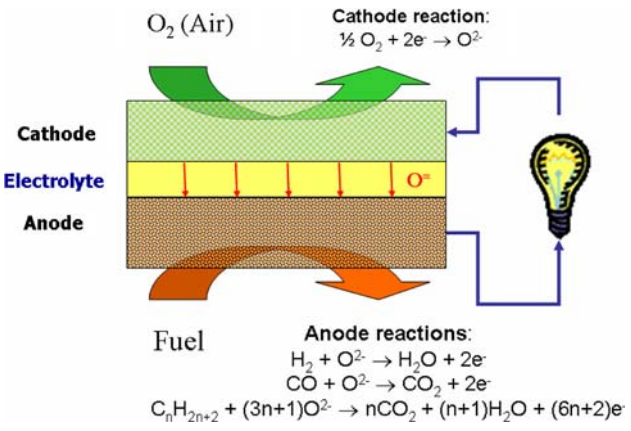

Fig. 1 Schematic diagram of a SOFC

$$O_2 + 2V_O^{\bullet\bullet} + 4e^- = 2O_O^x \quad (1)$$

where in Kröger–Vink notation, $V_O^{\bullet\bullet}$ is an oxygen vacancy site and O_O^x is an oxygen ion on a regular oxygen lattice site in the Y_2O_3–ZrO_2 (YSZ) electrolyte. As illustrated by Eq. 1, the oxygen reduction reaction requires the presence of oxygen and electrons as well as the possibility for generated oxide ions to be transported away from the reaction site into the bulk of the electrolyte. When the electrode and electrolyte materials possess only electronic and ionic conductivity, respectively, such as Sr-doped $LaMnO_3$ (LSM) electrode and YSZ electrolyte, these criteria are fulfilled in the vicinity of the three-phase boundary (TPB) between the electrode, electrolyte, and oxidant gas. If the electrode material possesses mixed electronic and ionic conductivity, for example, Sr-doped $LaCoO_3$ (LSC), oxygen species may be transported through the bulk of the electrode and the reaction zone could be extended beyond the electrode/electrolyte interface. Adler gave an excellent review recently on the factors affecting the reaction sites and reaction process for the O_2 reduction reaction [4].

There has been significant progress in reducing the operation temperature of SOFC from traditional 1000 °C to intermediate temperature range of 600–800 °C. Decreasing the operation temperature brings both dramatic technical and economic benefits. The cost of SOFC system can be substantially reduced by using less costly metal alloys as interconnect [5]. Furthermore, as the operation temperature is reduced, system reliability and operational life increases, increasing the possibility of using SOFC for a wide variety of applications, including residential and automotive applications. On the other hand, reduction in operation temperature results in a significant increase in the electrolyte and electrode resistivity and the polarization losses. To compensate for the increase in ohmic losses at lower temperatures, electrolytes with higher ionic conductivity or thinner films are used [6]. In SOFCs based on thin electrolyte, the overall losses of the cell are generally dominated by the polarization losses for the O_2 reduction on the cathode [7]. This is partly due to the high activation energy and slow reaction kinetics for the O_2 reduction reaction when compared with the hydrogen oxidation reaction. Consequently the development of cathodes with high performance and high stability becomes increasingly critical for the intermediate-temperature SOFCs or ITSOFCs.

Among various cathode materials, lanthanum strontium manganite (LSM)-based perovskites are, till today, the most investigated cathode materials for SOFCs. Despite the prominent role of LSM, there is a lack of a comprehensive treatise on the development and technological achievement of this most important material of SOFC. This review encompasses the development, fundamental understanding, and achievements of LSM-based electrode materials in the last 20–30 years. The article will start with the review on the structure, oxygen nonstoichiometry, and defect model, followed by detailed discussion on electronic conductivity, thermal expansion coefficient, oxygen diffusion and ionic conductivity, and the interfacial reaction and compatibility of the LSM-based perovskite oxides with electrolyte and metallic interconnect. The polarization-induced activation, performance, and performance stability of LSM-based cathodes under SOFC operating conditions are examined.

Oxygen nonstoichiometry, defect model, and surface segregation

Structure and phase

Lanthanum manganite ($LaMnO_3$) and strontium-substituted lanthanum manganite ($La_{1-x}Sr_xMnO_3$) belong to ABO_3 perovskite oxide family. Ideal perovskite crystallizes in cubic close-packed lattice structure. Figure 2 shows the crystal structure of $La_{0.7}Sr_{0.3}MnO_3$. The larger rare earth ions (e.g., La) occupy the 12 coordinated A-sites and the transition metal ions (e.g., Mn) occupy the octahedral B-sites. Both the electrical conductivity and catalytic activity of lanthanum manganite are enhanced considerably when lanthanum is substituted partially with strontium. The stability of the perovskite oxide, in general, increases with the size of A-site cations. Thus, majority of the work has been performed on lanthanum-based perovskites, in particular the $LaMnO_3$-based series oxides.

Undoped $LaMnO_3$ is orthorhombic at room temperature and shows an orthorhombic/rhombohedral crystallographic transformation at ~600 °C [8]. This transformation has been attributed to the oxidation of some Mn^{3+} to Mn^{4+} ions, which reduces the energy tending to produce long-range Jahn–Teller ordering. Thus, the orthorhombic/rhombohedral transition temperature is dependent on the Mn^{4+} content and sensitive to the stoichiometry of the

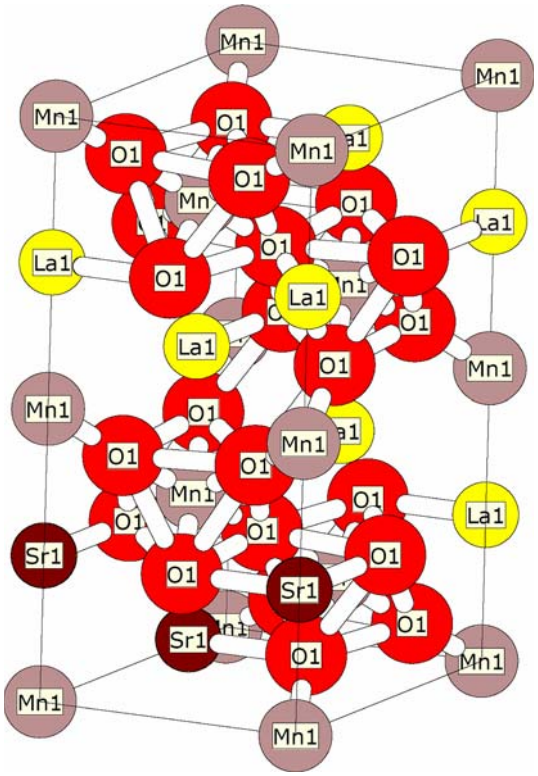

Fig. 2 Crystal structure of $La_{0.7}Sr_{0.3}MnO_3$ (courtesy of Dr Khuong P Ong of Institute of High Performance Computing, Singapore)

material. Doping lower-valence cations such as Sr^{2+} and Ca^{2+} for the La sites increases the Mn^{4+} concentration in $LaMnO_3$, thus affecting the transformation temperature.

Hammouche et al. [9] carried out a detailed study on the crystallographic and thermal properties of $La_{1-x}Sr_xMnO_3$ ($0 \leq x \leq 0.5$) in 1989. The radiocrystallographic study of the LSM samples was carried out by XRD using ultra-pure silicon as a standard element. Figure 3 shows the XRD patterns of $La_{1-x}Sr_xMnO_3$ with $x = 0.1$. A slight shift of all peaks in the direction of increasing diffraction angles was observed as the Sr doping level increased. Table 1 gives the refined interreticular distances d_{hkl} determined for

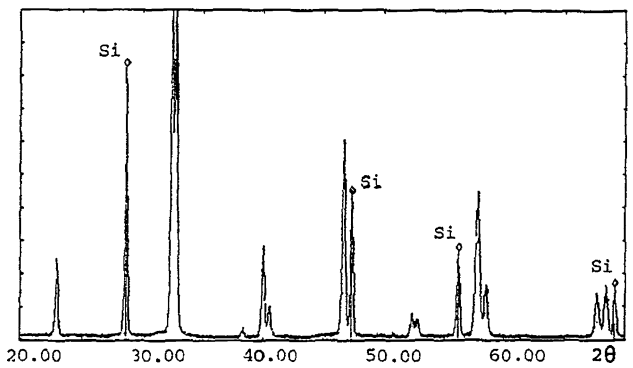

Fig. 3 XRD patterns of $La_{1-x}Sr_xMnO_3$ with $x = 0.1$, using ultrapure silicon as a standard after Hammouche et al. [9]

Table 1 X-ray diffraction results of $La_{0.9}Sr_{0.1}MnO_3$ after Hammouche et al. [9]

hkl	I/I_o	$d_{observed}$	$d_{calculated}$
012	25	3.895	3.893
110	100	2.765	2.767
104	99	2.740	2.740
202	28	2.255	2.255
006	10	2.226	2.226
024	61	1.9460	1.9467
122	9	1.7477	1.7481
116	7	1.7345	1.7344
300	29	1.5978	1.5974
214	46	1.5929	1.5921
018	18	1.5764	1.5766
220	15	1.3832	1.3834
208	17	1.3698	1.3698

the LSM sample shown in Fig. 3. All the XRD patterns are perfectly indexed in the hexagonal–rhombohedral system. The unit cell parameters, a_h and c_h, shows a dependence on the Sr substitution x. The a_h parameter decreases linearly with the composition for $x \geq 0.1$ while c_h does not exhibit measurable variations. The decrease of a_h with x may result from the much smaller size of Mn^{4+} compared to Mn^{3+}. Their effective ionic radii in octahedral coordination with oxygen are 0.53 and 0.645 Å, respectively [10]. The insensitivity of c_h with the Sr substitution has been explained by the fact that the Sr^{2+} ion (1.44 Å) is slightly larger than La^{3+} ion (1.36 Å). As they are located along the z-axis of the hexagonal unit, the contraction created by the Mn^{4+} cations could be compensated.

The structure of LSM has also been studied by others [11, 12]. Depending on the doping level, $La_{1-x}Sr_xMnO_{3-\delta}$ can display three lattice types: rhombohedral ($0 \leq x \leq 0.5$), tetragonal ($x = 0.5$), and cubic ($x = 0.7$) [11]. Zheng et al. [13] systematically studied the phase behavior of $La_{1-x}Sr_xMnO_3$ with various Sr doping content and A/B cation ratio. As the Sr content is increased to $x = 0.2$, the perovskite structure adopts an orthorhombic distortion, and changes to a monoclinic or hexagonal structure for $0.2 \leq x \leq 0.3$. When Sr content increases to 30 mol%, the structure reverts to orthorhombic symmetry. The influence of the A/B cation ratio on the changes in the lattice constants and cell volume of the perovskite phase is minor, as compared to the effect of Sr content. However, A/B cation ratio has significant effect on the minor phases formed. In the case of A/B < 1, the main minor phases observed were Mn_3O_4. When A/B = 1 and A/B > 1, the secondary phase La_2O_3 and its hydrated product $La(OH)_3$ were observed. $La(OH)_3$ is not a desirable phase in SOFC cathode materials due to its low melting point (~252 °C) and its tendency to swell and degrade the strength of the cathode.

Excess La_2O_3 is also known to react with YSZ to form a highly resistive lanthanum zirconate phase at the LSM/YSZ interface [14].

Oxygen nonstoichiometry and defect model

Lanthanum manganite is somewhat unusual in comparison to most perovskite oxides in that it can have the oxygen-excess as well as the oxygen-deficient nonstoichiometries. This is generally denoted by $La_{1-x}A_xMnO_{3\pm\delta}$ (A is divalent cation, such as Sr^{2+}, Ca^{2+}, "+" means oxygen excess and "−" means oxygen deficiency). Mizusaki et al. [15–19] investigated in detail the oxygen nonstoichiometry of $La_{1-x}Sr_xMnO_{3\pm\delta}$ as a function of oxygen partial pressure, P_{O_2}, temperature, and the composition. Figure 4 shows the oxygen nonstoichiometry of $La_{1-x}Sr_xMnO_{3\pm\delta}$ as a function of P_{O_2} and temperatures [17]. In addition to the oxygen-deficient region, the oxygen-excess region also appears as illustrated in Fig. 4a. For $LaMnO_3$ and $La_{1-x}Sr_xMnO_{3\pm\delta}$ with $x < 0.4$, the oxygen content exhibits two plateaus in its oxygen partial pressure dependence, one is around the oxygen excess $(3 + \delta)$ at high oxygen partial pressure and the other around the stoichiometric composition ($\delta = 0$) at intermediate oxygen partial pressures (10^{-5}–10^{-10} Pa)

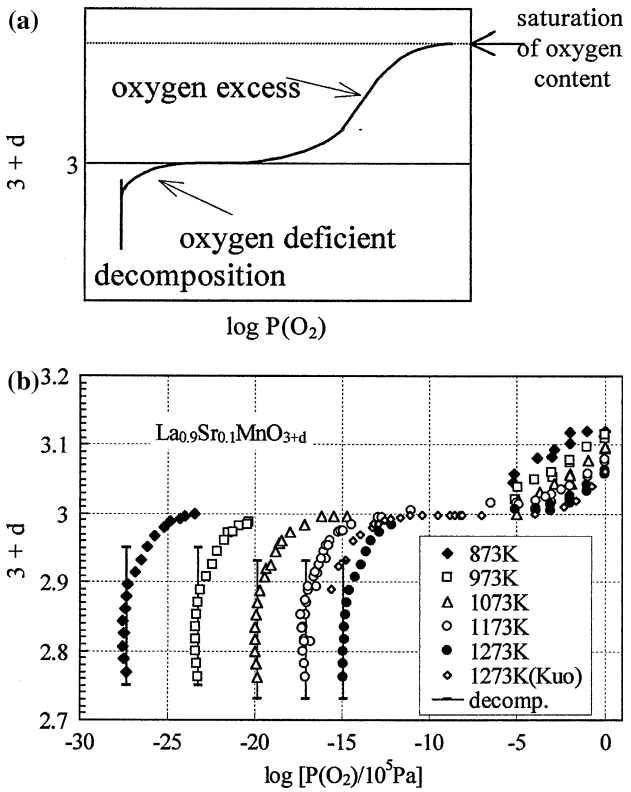

Fig. 4 Oxygen nonstoichiometry of $LaMnO_3$ as a function of oxygen partial pressure of oxygen. Upper curve: schematic representation of oxygen nonstoichiometry; lower curve: oxygen nonstoichiometry of $La_{0.9}Sr_{0.1}MnO_{3\pm\delta}$ after Mizusaki et al. [17]

(a typical example is given for $La_{0.9}Sr_{0.1}MnO_{3\pm\delta}$, Fig. 4b). At lower oxygen partial pressures, the oxides become oxygen deficient $(3 - \delta)$ and the charge compensation of the positive effective charges of $V_O^{\bullet\bullet}$ is maintained by Mn reduction. $La_{1-x}Sr_xMnO_{3\pm\delta}$ appears to be in oxygen-excess nonstoichiometry region under normal fuel cell operation conditions and becomes oxygen deficient only at very low partial pressure of oxygen, e.g., $<10^{-10}$ Pa at 900 °C for $x = 0.2$. The oxygen-excess nonstoichiometry of $La_{1-x}Sr_xMnO_{3+\delta}$ is most interesting as it is rarely observed in other perovskite-type oxides.

Various defect models have been proposed to explain the defect structure of doped $LaMnO_3$ oxides, particularly in the oxygen-excess region. At high oxygen partial pressure, in order to compensate for the electrical neutrality raised by Mn oxidation, there can be two possibilities of defect formations: the interstitial oxide ions or the cation vacancies. Neutron powder diffraction and high-resolution transmission electron microscopy (HRTEM) results indicate that cation vacancies, rather than oxygen interstitials, are responsible for the oxygen-excess nonstoichiometry [20–22]. This is consistent with the close-packed nature of perovskite lattice, which could not accommodate an excess of oxygen as an interstitial oxygen ion. Thus apparent oxygen excess can only be considered in terms of a Schottky-type disorder, which involves the formation of cation vacancies [23]. However, there are some disagreements in the literature concerning the ratio of La to Mn cation vacancies [20–22, 24]. Atomic simulation results indicate that oxidative nonstoichiometry leads to the formation of cation vacancies on both La and Mn sites with tendency toward more La vacancies [25].

To explain the upper limit of δ, van Roosmalen and Cordfunke [26–28] considered the charge disproportionation reaction of Mn^{3+} into Mn^{2+} and Mn^{4+} with a parameter ξ, i.e., the amount of Mn^{2+} and Mn^{4+} formed by the disproportion of Mn^{3+}. Since the La/Mn ratio is kept constant on incorporation of excess oxygen, the La site vacancy model inevitably requires occupation of the La ions on the Mn site according to [26–28]:

$$\begin{aligned} LaMnO_{3+\delta} + \frac{\delta}{2}O_2 &= \frac{3+\delta}{3}\left(La^{3+}_{1-2\delta/(3+\delta)}V_{2\delta/(3+\delta)}\right) \\ &\times \left(Mn^{3+}_{3(1-2\delta)/(3+\delta)}Mn^{4+}_{3.2\delta/(3+\delta)}La^{3+}_{\delta/(3+\delta)}\right)O_3^{2-} \end{aligned} \quad (2)$$

Upon dissolution of 3/2 oxygen molecules, six Mn^{4+} ions and two vacancies, i.e., one each at La and Mn site, are formed:

$$6Mn^x_{Mn} + 3/2O_2 \Leftrightarrow 6Mn^{\bullet}_{Mn} + 3O^x_O + V'''_{La} + V'''_{Mn} \quad (3)$$

where $Mn^{\bullet}_{Mn}$ and Mn^x_{Mn} are Mn^{4+} and Mn^{3+} ions, respectively.

Satisfactory results have been reported for the model in quantitatively explaining the relation between the Sr doping level, excess oxygen δ, and oxygen partial pressure [29]. Nevertheless, the model can only apply to the perovskite system in which charge disproportionation would occur. Mizusaki et al. [17] proposed a vacancy exclusion model to explain the upper limit of δ, in which a sphere of a vacancy exclusion space consisting of nine unit cells (nine La ions) and only a single La ion inside this sphere can enter into a Mn site to create a La site vacancy. This yields the upper limit of δ, $\delta_{max} = 3/17 = 0.1764$ [17]. The maximum oxygen excess can be determined from the maximum number of vacancy excluding spaces available in the lattice. This explains the observed disappearance of the oxygen excess region for LSM at $x > 0.4$. For $x > 0.4$, there is no room for the vacancy excluding space around the cation vacancies. A modified vacancy exclusion model was proposed by Nakamura and Ogawa [30] in which the first 6 and second 12 nearest neighboring La (Mn) sites around a La (Mn) site vacancy are excluded from the additional formation of vacancies.

Alonso et al. [22, 31] prepared $LaMnO_{3+\delta}$ with high δ values ($0.11 \leq \delta \leq 0.29$) by thermal decomposition of metal citrates by annealing at high oxidizing conditions of low temperature (800–1100 °C) and high oxygen pressure (200 bar). The neutron powder diffraction results revealed substantially higher proportion of Mn vacancies as compared to the La vacancies. This indicates that the ratio of the La/Mn vacancies would depend strongly on the preparation conditions.

In the oxygen-deficient region, the predominant ionic defect is the oxygen vacancy, $V_O^{\bullet\bullet}$. The charge neutrality is maintained by the reduction of transition element in B-site to the lower valence state. This can be represented as [17]:

$$\frac{1}{2}O_2 + V_O^{\bullet\bullet} + 2Mn_{Mn}^{x} \Leftrightarrow 2Mn_{Mn}^{\bullet} + O_O^{x} \quad (4)$$

$$\frac{1}{2}O_2 + V_O^{\bullet\bullet} + 2Mn_{Mn}^{\prime} \Leftrightarrow 2Mn_{Mn}^{x} + O_O^{x} \quad (5)$$

where $Mn_{Mn}^{\prime}$ is Mn^{2+} ion. Since the electronic conduction in $La_{1-x}Sr_xMnO_{3+\delta}$ is hopping-type and p-type irrespective of the oxygen content ($\delta < 0$ and $\delta > 0$), disproportion of Mn ion into Mn^{2+}, Mn^{3+}, and Mn^{4+} could occur. The reduction of the transition element in B-site to maintain charge neutrality also results in the increase of the average ionic radius of the cation and the consequent lattice expansion [32]. The isothermal expansion has an almost linear relationship with oxygen-deficit nonstoichiometry.

Nowotny and Rekas [23] derived defect-disorder models for undoped and Sr-doped $LaMnO_3$ and considered both a random-defect model and a cluster-defect model. In random-defect model, oxygen deficiency in $LaMnO_3$ is determined by the concentration of oxygen vacancies that are formed according to the following equilibrium:

$$Mn_{Mn}^{\bullet} + O_O^{x} \Leftrightarrow \frac{1}{2}O_2 + V_O^{\bullet\bullet} + Mn_{Mn}^{x} \quad (6)$$

Figure 5 shows the constructed random-defect model for undoped and Sr-doped $LaMnO_3$ as a function of oxygen partial pressure, P_{O_2} [23]. Concentration of oxygen vacancies ($[V_O^{\bullet\bullet}]$) in air is small and decreases sharply as the value of P_{O_2} increases. The addition of Sr results in the increased $[V_O^{\bullet\bullet}]$ and a rapid decrease in the concentration of cation vacancies. The oxygen nonstoichiometry and

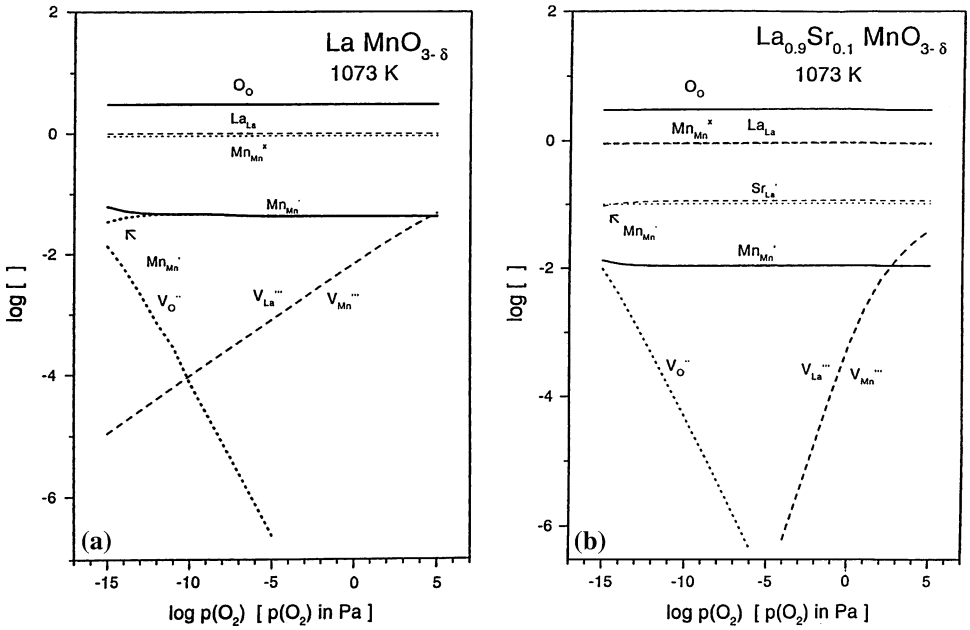

Fig. 5 Concentration of defects as a function of P_{O_2} in (**a**) undoped $LaMnO_3$ and (**b**) Sr-doped $LaMnO_3$, constructed by a random-defect model after Nowotny and Rekas [23]

electrical conductivity according to the random-defect model show a good agreement with the experimental data [33–35].

The formation of defect can also be expressed by the cluster model according to the following equilibrium [23]:

$$\mathrm{Mn}_{\mathrm{Mn}}^{\bullet} + \mathrm{Mn}_{\mathrm{Mn}}' + \mathrm{O}_{\mathrm{O}}^{x} \Leftrightarrow \frac{1}{2}\mathrm{O}_2 + \left(\mathrm{Mn}_{\mathrm{Mn}}' - V_{\mathrm{O}}^{\bullet\bullet} + \mathrm{Mn}_{\mathrm{Mn}}'\right) \tag{7}$$

The concentration of clusters has a substantial value only at very low P_{O_2} and, in general, the agreement between the cluster-defect model and experimental observation is poor.

The defect chemistry of $\mathrm{La}_{1-x}\mathrm{Sr}_x\mathrm{MnO}_{3\pm\delta}$ under cathodic polarization conditions has been subjected to intensive studies due to its importance in the fundamental understanding of the O_2 reduction mechanism and electrocatalytic activity. Yasumoto et al. [36, 37] studied the effect of oxygen nonstoichiometry on the electrocatalytic activity of a LSM cathode under polarization using impedance spectroscopy. The results suggest that oxygen nonstoichiometry affects the cathode reactivity under polarized and nonpolarized states through the exchange current density.

$$\sigma_{\mathrm{E}} = \beta\left(\frac{F}{RT}\right) \times P_{\mathrm{O}_2}^{1/2} \tag{8}$$

where σ_{E} is the electrode polarization conductivity or activity, and β (mA cm^{-2}) is proportional to the exchange current density and is a function of δ, T, and overpotential. β was found to increase linearly with decreasing δ at a constant polarization except under a large anodic overpotential [36].

Lee et al. [38] used in situ XPS measurement on $\mathrm{La}_{0.9}\mathrm{Sr}_{0.1}\mathrm{MnO}_3$ as a function of cathodic polarization. The XPS results showed the peaks of Mn 2*p* spectra were shifted to the lower binding energy as the applied potential became more cathodic, indicating the reduction of Mn ions. The oxygen reduction and the concomitant formation of Mn^{2+} ions and oxygen vacancies are proposed as:

$$2\mathrm{Mn}_{\mathrm{Mn}}^{\bullet} + \mathrm{O}_{\mathrm{O,LSM}}^{x} + V_{\mathrm{O,YSZ}}^{\bullet\bullet} + 2\mathrm{e} \rightarrow 2\mathrm{Mn}_{\mathrm{Mn}}^{x} + V_{\mathrm{O,LSM}}^{\bullet\bullet} + \mathrm{O}_{\mathrm{O,YSZ}}^{x} \tag{9}$$

$$2\mathrm{Mn}_{\mathrm{Mn}}^{x} + \mathrm{O}_{\mathrm{O,LSM}}^{x} + V_{\mathrm{O,YSZ}}^{\bullet\bullet} + 2\mathrm{e} \rightarrow 2\mathrm{Mn}_{\mathrm{Mn}}' + V_{\mathrm{O,LSM}}^{\bullet\bullet} + \mathrm{O}_{\mathrm{O,YSZ}}^{x} \tag{10}$$

For the oxygen reduction on LSM, there exists a significant hysteresis as shown by thermogravimetry studies of Hammouche et al. [39]. Chen et al. [40] also investigated the electrode behavior of $\mathrm{La}_{0.85}\mathrm{Sr}_{0.15}\mathrm{MnO}_3$ by cyclic voltammetry as a function of reverse potential at 900 °C and oxygen partial pressure of 0.001 atm. Based on the CV and potential responses in current step experiments, they considered that at the initial stage of the cathodic polarization, the reduction of Mn^{4+} to Mn^{3+} is accompanied by the removal of the cation vacancies.

$$V_{\mathrm{La}}''' + V_{\mathrm{Mn}}''' + 6\mathrm{Mn}_{\mathrm{Mn}}^{\bullet} + 3\mathrm{O}_{\mathrm{O,LSM}}^{x} + 3V_{\mathrm{O,YSZ}}^{\bullet\bullet} + 6\mathrm{e} \rightarrow 6\mathrm{Mn}_{\mathrm{Mn}}^{x} + 3\mathrm{O}_{\mathrm{O,YSZ}}^{x} \tag{11}$$

Further reduction of manganese ions and the generation of oxygen vacancies could take place only after all cation vacancies are consumed under cathodic polarization. However, the oxygen vacancy formation and the removal of cation vacancies may not be the only explanation for the hysteresis behavior as shown recently by Wang and Jiang [41].

Surface properties and segregation

The improved knowledge in surface segregation and surface properties of LSM-perovskites enhances our fundamental understanding of the electrocatalytic behavior and the oxygen reduction mechanism of LSM cathodes. The surface segregation of Sr is of particular interest as SrO affects the surface reactivity and the activation behavior of the LSM electrode. Jiang and Love [42] studied the activation behavior of $\mathrm{La}_{0.72}\mathrm{Sr}_{0.18}\mathrm{MnO}_3$ cathode after treatment of the LSM coating with a diluted HCl solution. The etched solution was analyzed by ICP-AES method. The results indicate that the acid etching primarily dissolved the LSM surface layers rather than the whole LSM particles. The high concentration of Sr in the etched solution indicates that Sr could be enriched on the LSM surface. The LSM electrode after the HCl treatment showed a much smaller activation effect as compared to that without the acid treatment [42].

Caillol et al. [43] investigated the effect of posttreatment and polarization on the surface segregation and chemisorbed oxygen species on $\mathrm{La}_{0.8}\mathrm{Sr}_{0.2}\mathrm{MnO}_3$ by XPS. The La/Sr ratios obtained for the initial and 1000 °C-sintered powders are identical to that expected from LSM stoichiometry. Sr enrichment was observed for screen-printed LSM sintered at 1200 °C with a La/Sr ratio of 2.4. However, after annealed at 800 °C in air for a week, the Sr segregation disappeared. This indicates that Sr migration is favored by the high temperature treatment. Low oxygen partial pressure and polarization (cathodic or anodic) all lead to the La/Sr ratios lower than 4. Sr segregation is also reported for $\mathrm{La}_{0.5}\mathrm{Sr}_{0.5}\mathrm{MnO}_3$ after heat treatment in an ultrahigh vacuum chamber at 600 °C [44]. Table 2 lists the observed Sr segregation at the surface of LSM reported in the literature. Segregation of Sr at the LSM surface appears to be a function of temperature, oxygen partial pressure, and polarization.

The marked segregation of Sr has also been observed for related perovskites, such as $\mathrm{La}_{1-x}\mathrm{Sr}_x\mathrm{VO}_3$ [45],

Table 2 Observation of Sr segregation at the surface of LSM

LSM	Treatment	Method	Sr segregation	References
$La_{0.72}Sr_{0.18}MnO_3$	Coating sintered at 1150 °C, air	HCl etching	Yes	[42]
$La_{0.8}Sr_{0.2}MnO_3$	Powder sintered at 1000 °C, air	XPS	Yes	[43]
	Coating sintered 1200 °C, air	XPS	Yes	[43]
	Sintered at 900 °C, low $p(O_2)$	XPS	Yes	[43]
	Sintered at 900 °C, high $p(O_2)$	XPS	No	[43]
	Cathodic polarization	XPS	Yes	[43]
	Anodic polarization	XPS	Yes	[43]
$La_{0.5}Sr_{0.5}MnO_3$	Heated at 600 °C, low $p(O_2)$	XPS	Yes, SrO	[44]

$La_{1-x}Sr_xCoO_3$ [46] and for layered perovskites, such as $La_{2-x}Sr_xNiO_4$ [47]. The intrinsic segregation of Sr species in the manganite, cobaltite, or nickelate phase is apparently strain driven because the ionic radius of the Sr^{2+} dopant is larger than that of the host La^{3+}. The dopant produces less elastic strain when accommodated at the surface rather than at bulk sites. Since Sr does not exist in a free state, the Sr-enriched regions are most likely in the form of SrO. An enhanced concentration of Sr is therefore available at the surface of these materials, which, as reviewed recently by Jiang [48], has significant effect on the polarization and activation behavior of LSM cathodes. As shown in Table 2, the SrO segregation on the surface of LSM grains is commonly studied by XPS technique even though the XPS averages over about ten atomic monolayers.

Electrical, thermal, and mechanical properties

Electronic conductivity and thermal expansion coefficient

LSM

$LaMnO_3$ is an intrinsic *p*-type conductor. Electronic conductivity is enhanced by substitution of the La^{3+} site with divalent ions such as strontium or calcium. Of the alkaline-earth dopants, Sr substitution is preferred for SOFC applications because the resultant perovskite forms stable compounds with high conductivity in the oxidizing atmosphere found at the cathode [34, 49]. When a La^{3+} ion at the A-site is replaced by a Sr^{2+} ion, an electric hole is formed on the B-site to maintain the electroneutrality, leading to the increased electrical conductivity:

$$LaMnO_3 \xrightarrow{x\mathrm{SrO}} La^{3+}_{1-x}Sr^{2+}_{x}Mn^{3+}_{1-x}Mn^{4+}_{x}O_3 \qquad (12)$$

Extensive data show that $La_{1-x}Sr_xMnO_3$, where $x = \sim 0.1$–0.2, provides high conductivity while maintaining mechanical and chemical stability with YSZ [34, 50].

Mizusaki [18] studied in detail the dependence of electronic conductivity and Seebeck coefficient of $La_{1-x}Sr_xMnO_3$ ($0 \le x \le 0.7$) as a function of P_{O_2}(i.e., the nonstoichiometry). Electronic conductivity increases with increase in x and the maximum electronic conductivity was obtained for $x = 0.5$. Zhang et al. [12] and Li et al. [11] also found that the electrical conductivity showed a peak value of 200–485 S/cm at $x = 0.5$ at 1000 °C. Figure 6 shows the plots of log σT against $1/T$ for $La_{1-x}Sr_xMnO_3$ ($0 \le x \le 0.7$) at pure oxygen ($P_{O_2} = 1$ bar) [18]. The plot for any composition falls on a straight line, suggesting that the conduction is by a small polaron hopping. The hopping conduction is generally expressed by [35]:

$$\sigma T = (\sigma T)^{\circ} \exp\left(-\frac{E_a}{kT}\right) = A\left(\frac{hv^{\circ}}{k}\right)c(1-c)\exp\left(\frac{E_a}{kT}\right) \qquad (13)$$

Here, $(\sigma T)^{\circ}$ and E_a are pre-exponential constant and activation energy, respectively, and c is the ratio of the carrier

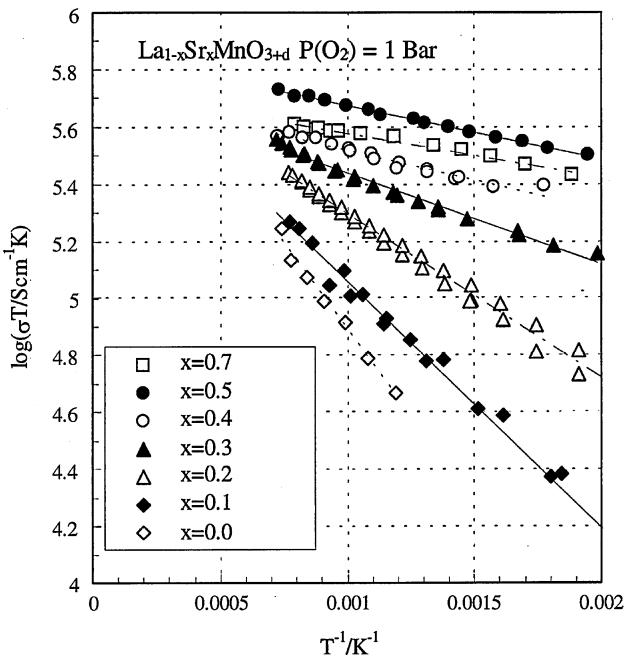

Fig. 6 Temperature dependence of electronic conductivity (σ) of $La_{1-x}Sr_xMnO_{3+d}$ ($0 \le x \le 0.7$) at pure oxygen ($P_{O_2} = 1$ bar) after Mizusaki et al. [18]

occupancy of the level on which the hopping conduction takes place. The conductivity is also a function of non-stoichiometry and partial pressure of oxygen. In the oxygen excess region (or high $P_{O_2} > 10^{-5}$ bar), σ is constant, while it decreases sharply with the decrease in oxygen content in the oxygen-deficient region (low $P_{O_2} < 10^{-5}$–10^{-10} bar) [18].

The electronic conductivity depends significantly on the preparation and crystalline structure of the LSM specimen. Li et al. [11] prepared LSM samples by conventional sintering and plasma spraying. Depending on the composition, the electronic conductivity of the sintered sample is between 40 and 485 S cm^{-1} at 1000 °C and that of plasma-sprayed coatings between 50 and 201 S cm^{-1}. The electronic conductivity of the plasma-sprayed samples is 50% lower than that of the sintered sample.

Porosity has a significant effect on the electrical conductivity of the LSM electrode. Otoshi et al. [51] studied the effect of porosity on the electrical conductivity of LSM coating at 800 °C and found that the electrical conductivity decreased from ~148 S cm^{-1} for 10% porosity to ~45 S cm^{-1} for 41% porosity. Mattiot et al. [52] measured the electrical conductivity of screen-printed $La_{0.83}Sr_{0.17}MnO_3$ coating. The porosity of the coating is in the range of 40% to 35% and the electrical conductivity is 21, 34, and 64 S cm^{-1} for the coating sintered at 1100, 1200, and 1300 °C, respectively. The increased electrical conductivity for the LSM coating sintered at high temperatures is due to the reduced porosity. For a screen-printed $La_{0.72}Sr_{0.18}MnO_3$ electrode, Jiang et al. [53] reported an electrical conductivity 34–56 S cm^{-1} in air at 800 °C.

For undoped $LaMnO_3$, the thermal expansion coefficient (TEC) is in the range of 11.33 × 10^{-6} to 12.4 × 10^{-6} K^{-1} [54, 55]. This is slightly higher than that of the most commonly used YSZ electrolyte, which is approximately 10.3 × 10^{-6} K^{-1} in the temperature range from 50 to 1000 °C in air or in H_2 atmosphere [56, 57]. However, the TEC value decreases with increasing A-site deficiencies in $La_{1-x}MnO_3$ and TEC of $La_{0.9}MnO_3$ is 10.55 × 10^{-6} K^{-1} in the temperature range from 1000 to 50 °C [55]. For Sr-doped $LaMnO_3$, the TEC varies between 11.2 and 12.7 × 10^{-6} K^{-1} [55, 58, 59].

Complete or partial replacement of lanthanum and/or manganese at the A- and/or B-site can significantly alter the electronic conductivity, TEC, chemical, and thermal stability with respect to the reaction with YSZ. Thus, various manganite-based perovskites have been studied as potential cathodes for ITSOFCs, including Ca-doped $LaMnO_3$ [55], Sr-doped $PrMnO_3$ and $NdMnO_3$ [60–63], Sr-doped $GdMnO_3$ [64, 65], Ce-doped $SrMnO_3$ [66], Co, Fe, and Ni-doped (La,Sr)MnO_3 [59, 67, 68], doped $YMnO_3$ [69, 70], and (La,Sr)(Cr,Mn)O_3 [71]. Detailed description of the alternative manganites would be out of scope of this review. Thus, for the purpose of comparison only the electronic conductivity and TEC of selected alternative manganite perovsites are given in Table 3.

LSM/YSZ composite

For LSM/YSZ composite cathode, the connectivity of the electronic conducting LSM and ionic conducting YSZ phases is crucial to produce a mixed conducting composite, because the ionic conductivity of LSM and the electronic conductivity of YSZ are negligible under normal SOFC operation conditions. Kim et al. [72] measured the resistance (R_Ω) of porous LSM/YSZ composites at 950 °C and found that abrupt increase of the resistance occurs when the YSZ content in the composite is higher than 50 wt.%. On dense LSM/YSZ composites with LSM content higher than 30 wt.%, the activation energy of the composite follows closely that of the electrical conductivity for pure LSM [73]. For the composite with LSM content of 30–40 wt.%, the composite has a higher oxygen ionic conductivity than pure LSM, but lower than YSZ. Yang et al. [74] found that when the LSM content in the LSM/YSZ composite is higher than 20%, the conduction is completely controlled by the LSM phase. Figure 7 compares the electronic conductivity and activation energy of LSM/YSZ composites. The threshold for the ionic connectivity in the LSM/YSZ composite is between 50 and 70 wt.% of YSZ phase depending on whether the composite is porous or dense.

Oxygen diffusion coefficient and ionic conductivity

Oxygen diffusion and surface exchange coefficients

Oxygen diffusion and transportation properties are very important for the oxygen reduction reaction at the electrode/electrolyte interface in SOFC. Among the elemental steps for the oxygen reduction reaction, there are at least two steps associated with oxygen diffusion: oxygen surface exchange between the electrode and gaseous phase, and surface and/or bulk diffusion of oxygen species. The oxygen diffusion and incorporation properties of LSM materials can be characterized by oxygen surface exchange coefficient (k) and oxygen chemical diffusion coefficient (D^*). The most common technique in the measurement of k and D^* is the $^{16}O/^{18}O$ isotope exchange measurement. In this method, the oxide sample is annealed in ^{18}O-enriched oxygen and the net isotope flux crossing an O_2/solid surface is directly proportional to the difference in isotope fractions between the gas and the solid. An oxygen tracer is introduced and sample is quenched. The isotope concentration profile in the sample is measured by secondary ion mass spectrometry (SIMS) and k and D^* parameters are obtained by fitting the experimental data.

Table 3 Thermal expansion coefficient, electrical conductivity, and activation energy of alternative manganite-based perovskite oxides

Composition	TEC	Conductivity		References
	$\times 10^{-6}$ K^{-1}	σ (S cm^{-1})	E_a (kJ mol^{-1})	
$LaMnO_3$	12.5	83 (800 °C)		[18, 55]
$La_{0.9}Sr_{0.1}MnO_3$	11.2	120 (800 °C)		[18, 55]
$La_{0.8}Sr_{0.2}MnO_3$	12.0	190 (900 °C)	14.4	[58]
$La_{0.6}Sr_{0.4}MnO_3$	12.7	320 (800 °C)		[18, 55]
$La_{0.7}Sr_{0.3}MnO_3$	11.7	178 (800 °C)		[60]
$La_{0.84}Sr_{0.16}MnO_3$	11.62	83 (800 °C)	11.61	[59]
$CaMnO_3$	17.5			[55]
$La_{0.8}Ca_{0.2}MnO_3$	10.0			[55]
$Pr_{0.7}Sr_{0.3}MnO_3$	10.6	146 (800 °C)		[60]
$Pr_{0.85}Sr_{0.15}MnO_3$	10.9	117 (700 °C)	8.71	[63]
$Pr_{0.5}Sr_{0.5}MnO_3$	12.9	250 (700 °C)	5.26	[63]
$Pr_{0.7}Sr_{0.3}MnO_3$	12.4	117 (800 °C)		[62]
$Nd_{0.7}Sr_{0.3}MnO_3$	10.3	269 (800 °C)		[60]
$Sm_{0.7}Sr_{0.3}MnO_3$	9.9	133 (800 °C)		[60]
$Gd_{0.7}Sr_{0.3}MnO_3$	9.5	83 (800 °C)		[60]
$Gd_{0.5}Sr_{0.5}MnO_3$	6.84[a]	229.5 (800 °C)	8.3	[64]
$Gd_{0.8}Sr_{0.2}MnO_3$	Very low, nonlinear	28		[65]
$Gd_{0.8}Sr_{0.2}MnO_3$	Negative	123.6 (800 °C)	20.6	[64]
$Pr_{0.7}Ca_{0.3}MnO_3$	11.9	148 (800 °C)		[62]
$Sr_{0.7}Ce_{0.3}MnO_3$	10.1	300 (900 °C)		[66]
$Gd_{0.8}Sr_{0.2}Co_{0.9}Mn_{0.1}O_3$	24	271 (800 °C)		[65]
$Gd_{0.8}Sr_{0.2}Co_{0.2}Mn_{0.8}O_3$	~10.5	28 (800 °C)		[65]
$Gd_{0.7}Ca_{0.3}Co_{0.7}Mn_{0.3}O_3$	~16.5	52 (800 °C)		[65]
$Gd_{0.7}Ca_{0.3}Co_{0.4}Mn_{0.6}O_3$	~10.5	37 (800 °C)		[65]
$Gd_{0.7}Ca_{0.3}MnO_3$	Very low, nonlinear	27 (800 °C)		[65]
$NdMnO_3$	4.55	71	25.6	[61]
$Nd_{0.7}Sr_{0.3}MnO_3$	12	200	12.5	[61]
$Nd_{0.5}Sr_{0.5}MnO_3$	13.6	316	6.4	[61]
$La_{0.84}Sr_{0.16}Mn_{0.8}Co_{0.2}O_3$	11.69	47 (800 °C)	17.98	[59]
$La_{0.84}Sr_{0.16}Mn_{0.6}Co_{0.4}O_3$	13.65	45 (800 °C)	23.69	[59]
$La_{0.84}Sr_{0.16}Mn_{0.8}Fe_{0.2}O_3$	11.58	37 (800 °C)	17.38	[59]
$La_{0.84}Sr_{0.16}Mn_{0.6}Fe_{0.4}O_3$	11.55	18 (800 °C)	19.77	[59]
$La_{0.76}Sr_{0.19}Mn_{0.7}Ni_{0.3}O_3$	14.05			[67]
$La_{0.82}Sr_{0.16}Mn_{0.7}Ni_{0.3}O_3$	11.7	68 (900 °C)	15.8	[68]
$YNi_{0.33}Mn_{0.67}O_3$		0.63 (300 °C)	27	[69]
$Y_{0.7}Ca_{0.3}MnO_3$	7.0	80 (800 °C)	18.3	[70]
$Y_{0.5}Ca_{0.5}MnO_3$	11	161 (800 °C)	9.6	[70]
$La_{0.75}Sr_{0.25}Cr_{0.5}Mn_{0.5}O_3$	12.0	25.3 (800 °C)	26.1	[71]
$La_{0.8}Sr_{0.2}Cu_{0.9}Mn_{0.1}O_3$	15.0	140 (900 °C)		[58]
$La_{0.8}Sr_{0.2}Cu_{0.4}Mn_{0.6}O_3$	13.0	50 (900 °C)	24	[58]
YSZ	10.3			[56]

[a] Estimated

Carter et al. [75] measured the oxygen diffusion coefficient and oxygen surface exchange coefficient of Sr-doped $LaMnO_3$ by SIMS technique. D^* increases with an increase in Sr doping on the A-site. For example, for $La_{0.65}Sr_{0.35}MnO_{3-\delta}$ D^* is 4×10^{-14} cm^2 s^{-1} at 900 °C and increases to 3×10^{-12} cm^2 s^{-1} for $La_{0.5}Sr_{0.5}MnO_{3-\delta}$. Increase in the A-site doping provides further oxygen vacancies. The activation energy of the oxygen self-diffusion coefficient is 300–350 kJ mol^{-1} for manganite-based perovskites [75]. This indicates that the association enthalpy, ΔH_a, resulting from the formation of complex defects, such as $[M'_{La} - V_O^{\bullet\bullet}]$, could be very high. The oxygen diffusion properties of $La_{0.8}Sr_{0.2}MnO_3$ have also been reported by De Souza et al. [76]. The diffusion of

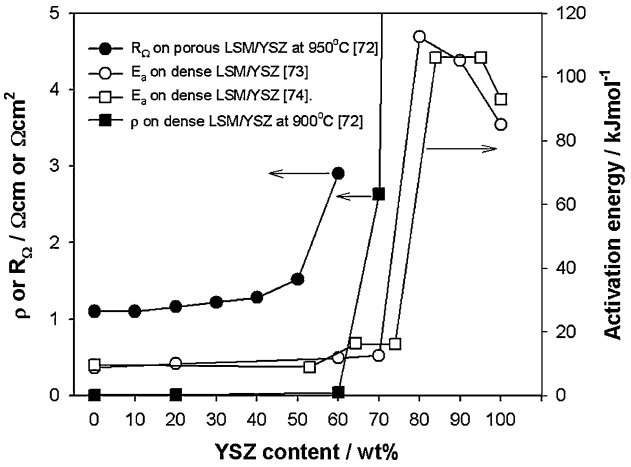

Fig. 7 Electronic conductivity and activation energy as a function of LSM/YSZ composite compositions. Numbers are references cited

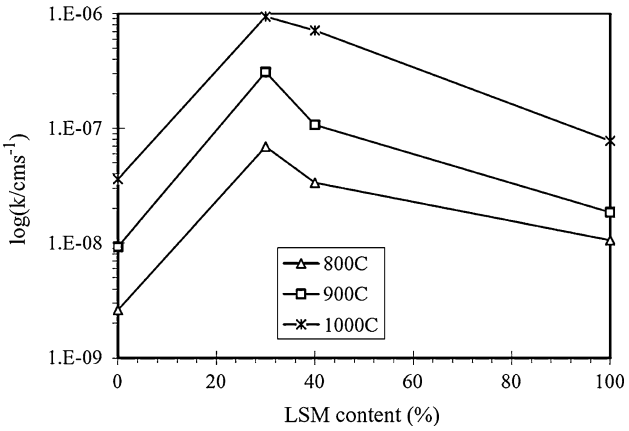

Fig. 8 Measured effective surface oxygen exchange coefficient of the LSM/YSZ composites as a function of the LSM content after Ji et al. [73]

oxygen along grain boundaries was found to be much faster than through the bulk. Nevertheless, the actual oxygen diffusion coefficient is very low due to the site fraction of oxygen vacancies.

The oxygen diffusion coefficient in La-deficient manganites, $La_{0.9}MnO_3$, is found to be comparable to that of stoichiometric $LaMnO_3$, as shown by Berenov et al. [77]. This observation is explained by the compensation of the formation of negatively charged La vacancies, V'''_{La}, by the oxidation of Mn ions rather than the formation of oxygen vacancies.

Horita et al. [78, 79] investigated the microstructure and oxygen diffusion at a dense LSM electrode and YSZ electrolyte interface. A gradual decrease of isotope oxygen concentration was observed in the $La_{0.9}Sr_{0.1}MnO_3$ layer followed by a flat profile at the interface. This indicates that the oxygen diffusion in the $La_{0.9}Sr_{0.1}MnO_3$ layer is slow. The TPB is characterized by a convex formation between LSM and YSZ with high concentration of manganese. The convex part shows high ^{18}O concentration, indicating the short oxygen diffusion at the TPB. At 1000 °C the D^* and k values of $LaMnO_3$ were found to be 2.45×10^{-13} cm^2 s^{-1} and 7.45×10^{-8} cm s^{-1}, respectively. For the $La_{1-x}Sr_xMnO_{3\pm\delta}$ ($x = 0.05$–0.20), D^* is of the order of 10^{-12}–10^{-11} cm^2 s^{-1} and oxygen ionic conductivity is estimated to be 10^{-7}–10^{-6} S cm^{-1} at 1000 °C [80]. Activation energy for the chemical diffusion of oxygen for LSM is in the range of 250–300 kJ mol^{-1} and close to 270 kJ mol^{-1} for $La_{0.9}Sr_{0.1}CoO_{3\pm\delta}$ in which oxide ions are transported by the vacancy diffusion mechanism [80]. This indicates that similar vacancy diffusion mechanism also applies to the LSM materials.

Ji et al. [73] investigated the electrical conductivity and oxygen diffusion properties of LSM/YSZ composites. The percolation threshold was identified at ~30 wt.% (or 28 vol%) of LSM. The oxygen diffusion coefficients of the composites with 30 and 40 wt.% LSM were much higher than that of the pure LSM, but they were slightly lower than that of the YSZ at the same temperature. The most interesting observation is that these two composites showed an enhanced effective surface exchange coefficient, i.e., greater than either of the parent materials, see Fig. 8. The result implies that both oxygen vacancies and electron concentrations are important for the surface exchange process. On the other hand, Yamahara et al. [81] measured the oxygen ion conductivity of porous YSZ network in the LSM/YSZ composite after the acid leaching of the LSM phase. They showed that the effective ionic conductivity of porous YSZ networks is significantly below that expected on the basis of the average porosity alone. The presence of LSM actually reduces the effective ionic conductivity of the YSZ in the LSM/YSZ composite. The reduced conductivity is attributed to the increase in the network interruptions and anomalously high constriction resulting from differential densification promoted by the presence of LSM.

Table 4 lists the oxygen diffusion coefficient and oxygen surface coefficient of undoped and doped $LaMnO_3$ as measured by SIMS techniques. As the incorporation and bulk diffusion of oxygen inside LSM cannot be expected to occur to a significant degree, the TPB becomes the reaction sites for the O_2 reduction.

The oxygen diffusivity of LSM materials has also been investigated by chemical diffusion measurements in an electrochemical cell using the potentiostatic step method [82, 83]. In the temperature range between 700 and 860 °C, the chemical diffusion coefficient of oxygen in $L_{0.79}Sr_{0.2}MnO_3$ was found to be in the range of 10^{-8}–10^{-6} cm^2 s^{-1} [82], significantly higher than that measured by SIMS. Similar chemical diffusion coefficient values are also reported by Badwal et al. on $La_{0.8}Sr_{0.2}MnO_3$ using a manometric method [84, 85]. The chemical diffusion

Table 4 Oxygen diffusion coefficient (D^*) and oxygen surface exchange coefficient (k) of LSM-based perovskites as measured by SIMS technique

Composition	Temperature (°C)	D^* ($cm^2\ s^{-1}$)	k ($cm\ s^{-1}$)	References
$LaMnO_3$	897	2×10^{-13}	7.7×10^{-8}	[77]
$La_{0.9}MnO_3$	897	1.2×10^{-13}	4.8×10^{-8}	[77]
$La_{0.92}MnO_3$	1000	2.45×10^{-13}	7.45×10^{-8}	[78]
$La_{0.65}Sr_{0.35}MnO_3$	900	4×10^{-14}	5×10^{-8}	[75]
$La_{0.5}Sr_{0.5}MnO_3$	900	3×10^{-12}	9×10^{-8}	[75]
	800	8×10^{-14}	1×10^{-7}	[75]
	700	2×10^{-15}	1×10^{-8}	[75]
$La_{0.95}Sr_{0.05}MnO_3$	900	2.44×10^{-13}		[80]
$La_{0.90}Sr_{0.10}MnO_3$	1000	4.78×10^{-12}		[80]
$La_{0.80}Sr_{0.20}MnO_3$	1000	1.33×10^{-11}		[80]
	900	1.27×10^{-12}		[80]
$La_{0.80}Sr_{0.20}MnO_3$	1000	6.6×10^{-13}	5.62×10^{-8}	[76]
	900	1.6×10^{-13}	1.78×10^{-8}	[76]
	800	4.0×10^{-15}	5.62×10^{-9}	[76]
	700	3.1×10^{-16}	1.01×10^{-9}	[76]
YSZ-40 wt.%LSM	900	6×10^{-9}	1×10^{-7}	[73]
	800	1×10^{-9}	7×10^{-7}	[73]

coefficient is strongly dependent on oxygen nonstoichiometry, suggesting that the oxidation kinetics is either affected by a segregation-induced surface diffusion resistance during oxidation or by different defect concentration accompanying oxidation and reduction. In the chemical diffusion measurements, samples of high density (e.g., greater than 95%) are required as the measurements will be affected by fast gas phase transport down the pores. In addition, chemical diffusion experiments on LSM are complicated by the fact that, at high oxygen partial pressure, LSM exhibits oxygen excess [33], which is accommodated by metal vacancies [8, 20]. Thus, changes in chemical composition during chemical diffusion measurements may involve cation diffusion. This may cause some uncertainties in the analysis of chemical diffusion data obtained at high temperatures.

Ionic conductivity

Ionic conduction of LSM is due to the oxygen vacancy in oxygen lattice. These vacancies can be produced by (a) substitution of La^{3+} by Sr^{2+} and (b) partial oxidation of Mn^{4+} to Mn^{3+} or Mn^{3+} to Mn^{2+} [26, 34]. Ionic conductivity can be measured by methods such as dc polarization using a Hebb–Wagner cell and the four-probe technique using electron-blocking electrodes. Thin slices of YSZ with thickness of <300 μm are usually used as electron-blocking electrodes in the dc four-probe technique. In Hebb–Wagner technique, the oxygen ionic conductivity can be calculated by the Hebb–Wagner equation if the rate determining step of cathodic reaction on/in dense electrodes is the chemical diffusion of oxygen ion [86].

Using the Hebb–Wagner technique, Endo et al. [87] obtained 5.9×10^{-8} S cm^{-1} for the ionic conductivity of a $La_{0.9}Sr_{0.1}MnO_3$ sample at 800 °C. Ullmann et al. [88], using the same technique at the same temperature, found 1.7×10^{-4} S cm^{-1} for $La_{0.65}Sr_{0.35}MnO_3$, which is much higher than that reported by Endo et al. [87]. In this case, the ionic conductivity was calculated from the permeation fluxes through a dense LSM pellet.

Godoi et al. [89] measured the electronic and ionic conductivity of $La_{0.7}Sr_{0.3}MnO_3$, $Ce_{0.8}Y_{0.2}O_2$ (YDC), and LSM/YDC composites by the dc four-probe techniques. The samples were sintered at 1400 °C for 2 h and the density varied from 98% for YDC and 84% for LSM/YDC with 30 wt.% LSM. The conductivity measured with the YSZ electron-blocking electrodes is five orders of magnitude lower than that measured with Pt electrode, indicating that the conductivity measured with the electron-blocking electrodes represents the ionic conductivity. The ionic conductivity increases with the increase of YDC content in the LSM/YDC composites. Yasuda et al. [80] estimated the ionic conductivity of LSM using the measured oxygen tracer diffusion coefficient and the oxygen vacancy diffusion coefficient.

Table 5 summarizes the ionic conductivities of LSM-based cathode materials. The variations in ionic conductivity values may be related to the significant differences in the samples prepared and techniques used. The very low oxygen ionic conductivity of LSM is considered to be the

Table 5 Ionic conductivity (σ_i) and activation energy (E_a) of LSM-based perovskites

Composition	Temperature (°C)	σ_i (S cm^{-1})	E_a (eV)	Density (%)	References
$La_{0.95}Sr_{0.05}MnO_3$	900	1.10×10^{-7}		>97	[80][a]
$La_{0.90}Sr_{0.10}MnO_3$	1000	2.09×10^{-6}		>97	[80][a]
$La_{0.80}Sr_{0.20}MnO_3$	1000	5.76×10^{-6}		>97	[80][a]
	900	5.93×10^{-7}		>97	[80][a]
$La_{0.9}Sr_{0.1}MnO_3$	800	5.9×10^{-8}			[87][b]
$La_{0.65}Sr_{0.35}MnO_3$	800	1.7×10^{-4}		>93	[88][b]
$La_{0.7}Sr_{0.3}MnO_3$	800	6.3×10^{-4}	0.50	84	[89][c]
YDC-70 wt.%LSM	800	8.3×10^{-3}	0.97	83	[89][c]
YDC-30 wt.%LSM	800	1.4×10^{-2}	0.93	95	[89][c]
$Ce_{0.8}Y_{0.2}O_2$	800	7.2×10^{-2}		98	[89][c]
YSZ-40 wt.%LSM	900	3×10^{-3}			[73]
$Pr_{0.65}Sr_{0.3}MnO_3$	800	3.4×10^{-4}	1.19	>93	[88][b]
$Pr_{0.65}Sr_{0.3}Mn_{0.8}Co_{0.2}O_3$	800	4.4×10^{-5}	0.81	>93	[88][b]
$La_{0.75}Sr_{0.2}Mn_{0.8}Co_{0.2}O_3$	800	3.1×10^{-5}		>93	[88][b]

[a] By calculation

[b] By Hebb–Wagner technique

[c] By dc four-probe electron-blocking technique

main factor for the high polarization losses of LSM cathode for the O_2 reduction reaction in ITSOFC [90].

Mechanical properties

Mechanical property measurements for SOFC materials have not received a great deal of attention. This is particularly true for LSM materials. Meixner and Cutler [91] studied the mechanical properties of LSM. Figure 9 shows Young's modulus for $La_{1-x}Sr_xMn_{0.96}Co_{0.04}O_3$ (LSMC) samples at room temperature as a function of x after sintering at either 1400 °C or 1500 °C [91]. The characteristic strength also shows a strong dependence on the composition. It varied between 242 MPa for $x = 0.1$ to 58.7 for $x = 0.5$. LSMC compositions with high Sr concentration

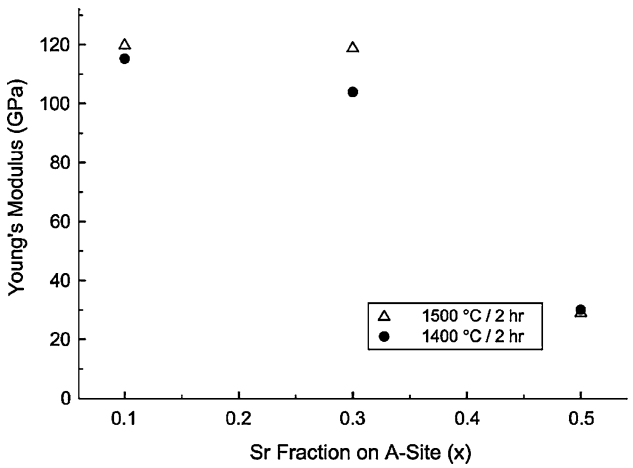

Fig. 9 Young's modulus measured using a resonant frequency technique for $La_{1-x}Sr_xMn_{0.96}Co_{0.04}O_3$ samples at room temperature as a function of x after sintering at either 1400 or 1500 °C after Meixner and Cutler [91]

($x = 0.5$) displays very low Young's modulus and low fracture strength. Atkinson and Selcuk [92] also reported a low biaxial flexure strength of ~50 MPa at room temperature for $La_{0.8}Sr_{0.2}MnO_3$. On the other hand, D'Souza and Sammes [93] determined a modulus of rupture of 164 MPa for $La_{0.875}La_{0.125}MnO_3$ at room temperature. This indicates that similar compositions of LSM do not always show low strength. Since strength is sensitive to processing, it is possible to obtain a wide range of strength values for the same composition. Thus it is difficult to compare strength data from the literature since flaw size controls strength and different flaw distribution is easy to form by different processing. Nevertheless, Young's modulus is relatively insensitive to processing, since it is dependent on bonding at an atomic level and is not controlled by flaw size.

The interaction between LSM and environmental factors during sample cooling appears to be critical to mechanical properties. Meixner and Cutler [94] studied in detail the plastic deformation of LSM and found that plastic deformation of LSM increased with increasing Sr on the A-site and displayed a strong dependence on processing history, and in particular on cooling rate. Slower cooling rate results in more deformation. LSM is known to display both oxygen excess and deficient nonstoichiometry depending on temperature, acceptor dopant level, and oxygen partial pressure. The degree of oxygen nonstoichiometry in LSM influences the absorption of oxygen during cooling and the importance of cooling rate is consistent with the LSM system in which the oxygen ion mobility is sufficient at high temperatures (1400 °C) to allow equilibrium conditions to prevail. At ambient temperatures, oxygen ion mobility is very low and the cooling rate determines the amount of time the sample equilibrates at intermediate temperatures. Thus, structural changes

associated with the nonstoichiometry of LSM may be caused by the uptake of oxygen during cooling.

Interaction and reactivity with other SOFC components

Solid-state reaction between two components occurs when sufficient energy is supplied to destabilize the parent system. The energy required to induce the reaction depends on the stability of the reactant and product phases. Perovskite oxides are active and they readily react with other fuel cell components, especially with yttria-zirconia electrolyte and chromium-containing interconnect materials at high temperatures. However, the relative reactivity of the cathodes at a particular temperature and the formation of different phases in SOFC operation environment critically depend on the nature of the cations presented in A- and B-site. Chemical compatibility and stability of perovskite-based materials are important due to the high operation and even higher fabrication temperatures of the SOFC components.

Interaction with the electrolyte

Interaction with YSZ electrolyte

The reactivity between LSM and the electrolyte (usually YSZ) has been extensively studied both experimentally and theoretically. Yokokawa et al. [95–97] examined the thermodynamic stability of various perovskite phases with respect to reaction products in the presence of zirconia, providing a framework for understanding the chemical compatibility and the thermodynamic driving force behind the formation of the phases between electrode and electrolyte. For example, their thermodynamic calculations have suggested that the formation of $La_2Zr_2O_7$ at the electrode–electrolyte interface will be high when (La + Sr) content at the A-site is $>Mn^{3+}$ ions at B-site and when Sr/La ratio is <0.43. High Sr content leads to Sr depletion from the lattice and eventual $SrZrO_3$ formation. The sub-stoichiometry at the A-site can help to prevent the depletion of A-site cations but Mn^{3+} ion activity is greatly enhanced when A-site deficiency is >0.15 (i.e., {(La + Sr)/Mn} < 0.85). Under such condition the dissolution of manganese in YSZ electrolyte is very high. Thermodynamic calculations show that A-site-deficient LSM can also prevent the formation of pyrochlore at the interface. Readers having a detailed interest in this topic are encouraged to read a recent review by Yokokawa [98]. This article will mainly focus on the experimental aspects of the chemical interaction and compatibility of cathode materials with YSZ electrolyte and its effect on the performance.

The interaction and interface phase formation between the LSM electrode and YSZ electrolyte vary with the stoichiometric composition of LSM [99, 100], the La/Sr ratio at the A-site [101] and the temperature and atmosphere of the heat treatments [102, 103]. Taimatsu et al. [104] studied the reaction of $La_{1-x}Ca_xMnO_3$ ($x = 0, 0.1, 0.2$) with YSZ in the temperature range of 1300–1425 °C. The proposed mechanism suggests that the reaction proceeds by the unidirectional diffusion of Mn into YSZ and, as a result, LSM at the interface becomes deficient in Mn and excess in La, leading to the formation of $La_2Zr_2O_7$ layer at the interface. The substitution of Ca for La in $LaMnO_3$ suppresses the manganese migration, thus reducing the reactivity with YSZ. Mitterdorfer and Gauckler [100] investigated in detail the mechanism of the formation of $La_2Zr_2O_7$ as a function of stoichiometry composition of LSM. Excess lanthanum oxide within the perovskite reacts immediately with YSZ to form dense $La_2Zr_2O_7$, characterized by the formation of cubic islands at the interface. The growth of $La_2Zr_2O_7$ is controlled by bulk diffusion of cations. Tricker and Stobbs [105] observed the formation of $La_2Zr_2O_7$ at the interface between $La_{0.85}Sr_{0.15}MnO_3$ and YSZ at 1000 °C. Jiang et al. [106] also observed the formation of $La_2Zr_2O_7$ at the interface between $La_{0.80}Sr_{0.2}MnO_3$ and YSZ at 1150 °C but not between A-site nonstoichiometry $(La_{0.80}Sr_{0.2})_{0.9}MnO_3$ and YSZ at the same temperature.

Lanthanum-deficient manganite, $La_{1-x}MnO_3$ ($x = 0$–0.2), is shown to be less reactive with YSZ than the stoichiometric one [107, 108]. Mori et al. [109] studied the reaction mechanism between $La_{0.9}MnO_3$ and YSZ at the temperature range between 1250 and 1400 °C. The induction period for the formation of $La_2Zr_2O_7$ was found to increase with the increase of the yttrium content in YSZ. The fundamental reason for the beneficial effect of A-site nonstoichiometry or Mn excess of LSM in the inhibiting of the lanthanum zirconate formation is most likely due to the fact that Mn_3O_4 does not equilibrate with lanthanum zirconate at high temperatures [110].

Manganese has high solubility in YSZ, ranging from ~11.4% at 1300 °C to 5.1% at 1000 °C. After cofiring YSZ with $La_{0.7}Sr_{0.3}Mn_{1.1}O_{3+x}$ at 1300 °C, Mn was observed to a depth of 20 μm in YSZ [111]. The manganese ions in YSZ are found to be only in divalent (about 80%) and trivalent (about 20%) states. No Mn^{4+} ions were detected in YSZ lattice, suggesting that Mn^{3+} ions are reduced when manganites are kept in contact with YSZ. Waller et al. [112] determined the diffusion coefficients of manganese in single crystal and polycrystalline YSZ in the temperature range of 1100–1400 °C. The effective diffusion coefficient of manganese in polycrystalline YSZ is far higher than that in single-crystal YSZ, indicating that grain boundary diffusion is the dominant transport process of Mn in polycrystalline YSZ. The activation energy for Mn diffusion in single crystal and polycrystalline YSZ was found to be 5.36 and 7.34 eV, respectively.

Mn activity is especially high when there is a deficiency at the A-site in perovskites. The diffusion of Mn into YSZ causes Mn depletion of the LSM and in the case of stoichiometric LSM chemically active La_2O_3 is formed, leading to the formation of $La_2Zr_2O_7$ at the interface. This is supported by the observation of the formation of pyrochlore in 75%YSZ/25%LSM and not in 20%YSZ/80%LSM mixtures sintered at 1300 °C for 2 h [113]. Excess of Mn in LSM/YSZ could delay or impede the formation of La_2O_3 at the interface. On the other hand, there is hardly detectable La in the YSZ, indicating very low solubility of lanthanum in YSZ.

Yamamoto et al. [114] examined the influence of the yttria content in ZrO_2 on the interface reactions and observed that zirconia with a high content of yttria (12 mol%) is less active with $La_{0.9}MnO_3$ than that with a low yttria content (8 mol%). Van Roosmalen and Cordfunke [115] studied the interaction between 3 mol% Y_2O_3-ZrO_2 (3YSZ) and LSM dense pellets, and found that 3YSZ is more reactive than 8 mol% Y_2O_3-ZrO_2 (i.e., yttria fully stabilized zirconia, YSZ) in the formation of pyrochlore phase with LSM. Jiang et al. [110] also studied the chemical interaction between LSM and 3YSZ electrolyte over the temperature range of 1300–1500 °C in air. Figure 10 is the SEM micrographs of a cross section of a LSM/3YSZ specimen after heat treatment at high temperatures [110]. Two distinct reaction layers are formed between the LSM coating and 3YSZ electrolyte, marked as "L1" and "L2" in the figure. EDS and XRD analysis results indicate that "L1" reaction layer is due to the formation of lanthanum zirconate pyrochlore phase, while "L2" reaction layer is primarily the cubic zirconia solid solution formed at the LSM/3YSZ interface. Similar results were also reported on the chemical interaction between (Pr,Sr)MnO_3 and 3YSZ [116]. The results indicate that the formation of the fluorite-type zirconia phase is mainly due to the dissolution of Mn ions into 3YSZ, while the interaction of La ions with 3YSZ causes the formation of $La_2Zr_2O_7$ pyrochlore phase.

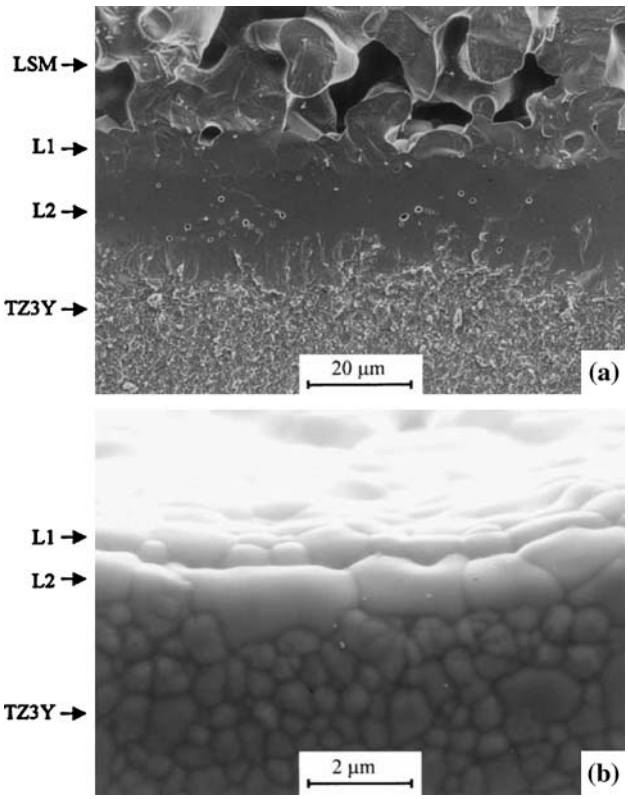

Fig. 10 SEM micrographs taken from (**a**) a fractured cross section of a LSM/3YSZ specimen after heat treatment at 1500 °C, and (**b**) a polished and thermally etched cross section of a LSM/3YSZ specimen after heat treatment at 1400 °C after Jiang et al. [110]

Phase studies in the $(Zr,Y)O_2$–La_2O_3–Mn_3O_4 system show that the fluorite-type cubic zirconia phase, rather than 3YSZ phase, is in equilibrium with LSM perovskite at high temperatures [110]. Figure 11 is the ternary phase diagram of $(Zr,Y)O_2$–La_2O_3–Mn_3O_4 system at 1400 °C based on the powder mixture experiments [110]. In the diagram, symbols "+" are the experimental data; $(Zr,Y)O_2$ represents the 3YSZ phase and La_yMnO_3 represents the perovskite phase due to its nonstoichiometry on the A-site. The phase relation agrees very well with the theoretical phase diagram of the ZrO_2–La_2O_3–Mn_3O_4 system at 1300 °C [97]. The phase diagram basically shows that the tetragonal 3YSZ cannot be in equilibrium with LSM perovskite at high temperatures and fluorite-type cubic zirconia solid solution phase, c-$(Zr,Mn,La,Y)O_2$, can be in equilibrium with the LSM perovskite phase. Thus from the phase stability point of view, partially stabilized zirconia such as 3YSZ may not be an optimum choice as the electrolyte materials in SOFC. The interaction between LSM and YSZ was also studied by others [109, 117, 118].

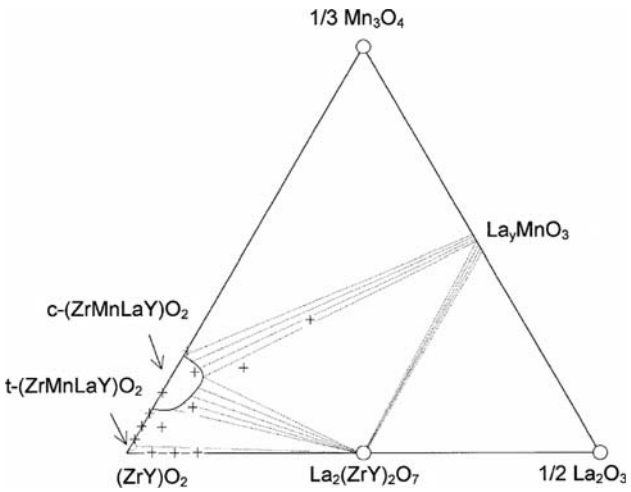

Fig. 11 Ternary phase diagram of $(Zr,Y)O_2$–La_2O_3–Mn_3O_4 system at 1400 °C in air. $(Zr,Y)O_2$ denotes 3 mol% Y_2O_3-ZrO_2. Symbols "+" are the experimental data after Jiang et al. [110]

The formation of $La_2Zr_2O_7$ phase at the LSM electrode/YSZ electrolyte interface is detrimental to the electrochemical activity and performance of the electrode [103, 119]. Brugnoni et al. [103] studied the growth coefficient and electrical resistivity of the $La_2Zr_2O_7$ layer in the case of $La_{0.85}Sr_{0.15}MnO_3$ electrode. The formation of $La_2Zr_2O_7$ layer was observed at the sample treated at 1200 °C. The growth of the reaction layer, i.e., $La_2Zr_2O_7$ is associated with La diffusion, rather than Mn diffusion. The growth coefficient obeys the Arrhenius relation. By extrapolation at the SOFC operation temperature (1000 °C), the film growth rate, D, is 8×10^{-18} cm^2 s^{-1}. Using the Wagner equation [120], $d^2 = Dt$, where d is the average thickness as a function of the annealing time t, the growth time of 1-μm-thick layer of $La_2Zr_2O_7$ at the interface would be 350,000 h. Thus, the major $La_2Zr_2O_7$ growth at the LSM/YSZ interface would be expected during the sintering process of the electrode. The electrical conductivity of the $La_2Zr_2O_7$ layer is 2×10^{-4} S cm^{-1} at 1000 °C. Slightly lower conductivity value of 10^{-4}–10^{-5} S cm^{-1} was reported for the strontium zirconates $SrZrO_3$, $Sr_4Zr_3O_{10}$, $Sr_3Zr_2O_7$, and Sr_2ZrO_4 and the lanthanum zirconates on sintered samples at 1000 °C [121]. This is significantly lower than the conductivity of 0.185 S cm^{-1} at 1000 °C for YSZ electrolyte [122]. The thermal expansion coefficient of $La_2Zr_2O_7$ was reported to be 9.2×10^{-6} K^{-1} also lower than 10.3×10^{-6} K^{-1} for 8YSZ electrolyte [109].

Sakaki et al. [60] studied the reactivity of $Ln_{1-x}Sr_xMnO_3$ (Ln = La, Pr, Nd, Sm, and Gd; $0 \leq x \leq 0.5$) with YSZ at a temperature range of 1000–1400 °C in air. The formation of the pyrochlore phase, $Ln_2Zr_2O_7$, is suppressed with the decrease of the size of Ln^{3+}. From the viewpoint of the reactivity with YSZ, $Pr_{1-x}Sr_xMnO_3$ and $Nd_{1-x}Sr_xMnO_3$ are the most stable. Takeda et al. [123] studied the reactivity between $Gd_{1-x}A_xMnO_3$ (A: Sr and Ca) and YSZ and found that $Gd_{1-x}A_xMnO_3$ shows much better stability with YSZ although the cathodic activity and electrical conductivity are similar to that of lanthanum manganite counterpart. On the other hand, Yoon et al. [64] reported the formation of a $SrZrO_3$ phase for the $Gd_{1-x}Sr_xMnO_3$/YSZ system heated at 1300 °C for 48 h.

Interaction with LSGM and GDC electrolyte

In addition to the YSZ electrolyte, the interaction and diffusion between SOFC cathode and other electrolytes are also reported. Huang et al. [124] studied the chemical reactions between the $La_{0.84}Sr_{0.16}MnO_3$ (LSM) and $La_{0.5}Sr_{0.5}CoO_3$ (LSC) cathodes, and $La_{0.9}Sr_{0.1}Ga_{0.8}Mg_{0.2}O_3$ (LSGM) electrolyte. Significant interdiffusion of Co into LSGM electrolyte and Ga into LSC was found at the LSC/LSGM interface at relatively low fabrication temperatures (e.g., 1050 °C for 2 h). In contrast, only small interdiffusion of Mn into LSGM and Ga into LSM was detected at the LSM/LSGM interface even though it was fired at 1470 °C. Naoumidis et al. [125] investigated the chemical interaction between $La_{0.75}Sr_{0.25}Mn_{0.8}Co_{0.2}O_3$ and $Pr_{0.8}Sr_{0.2}Mn_{0.8}Co_{0.2}O_3$ cathodes and LSGM electrolyte at 1300 °C. The transport of the Co from the perovskite cathode into the LSGM electrolyte is substantial and a distinct concentration of Co down to a depth of more than 100 μm was observed for the specimen sintered at 1300 °C for 100 h. The Mn diffusion into the electrolyte is less pronounced. Similar conclusion has also been drawn by Pelosato et al. [126] for the LSM and LSGM system. The change in the composition due to the Co and Mn diffusion into the LSGM electrolyte could also lead to the change in the electrical properties of the electrolyte. As shown by Ullmann et al. [127], the substitution of Co for Ga in the LSGM electrolyte increases the ionic conductivity and also introduces the mixed conducting behavior. Considering the small interdiffusion reactions between LSM and LSGM and similar thermal expansion coefficients, LSM is an appropriate cathode material for LSGM-based fuel cells.

The interaction between the LSM electrode and GDC electrolyte is sparsely reported. LSM and manganite-based perovskites such as $Nd_{1-x}Sr_xMnO_3$ ($0 \leq x \leq 0.5$) [61] show very good chemical stability with GDC electrolyte. Yoon et al. [64] heated the $Gd_{1-x}Sr_xMnO_3$/GDC system at 1300 °C for 48 h and found no reaction between GSM electrode and GDC electrolyte.

Interaction with Fe–Cr alloy metallic interconnect

One important issue in the development of ITSOFCs based on metallic interconnect is the interaction between the metallic interconnect and the cathode. Metallic interconnect such as chromia-forming alloys (e.g., stainless steel) generates volatile Cr-containing species at high temperatures in oxidizing atmospheres. Without effective protective coatings, the gaseous chromium species can lead to a rapid degradation of the SOFC performance due to the chemical interaction of Cr species at the Sr-doped $LaMnO_3$ (LSM) cathode side [128–130]. Figure 12 shows the typical polarization curves for the O_2 reduction reaction on a LSM cathode in the presence of a Fe–Cr alloy metallic interconnect at 900 °C. The rapid increase in the cathodic polarization for the reaction in the presence of a Fe–Cr alloy indicates the poisoning effect of the Cr species on LSM cathodes.

Taniguchi et al. [129] studied the interaction reaction between LSM and Inconel 600 (16%Cr, 8%Fe, and 76% Ni) at 1000 °C in air. The increase in cathodic polarization was found to be related to the intensity and amount of Cr at the cathode/electrolyte interface region. Similar degradation phenomena on LSM cathodes were also reported by others [128, 131]. It was also reported that the deposition of

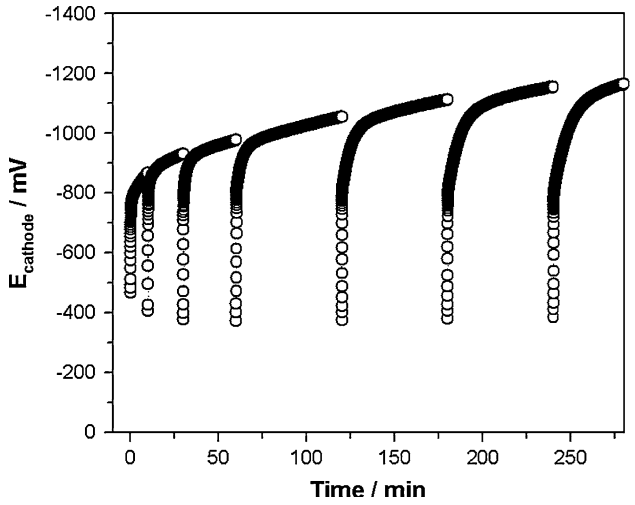

Fig. 12 Polarization curves for the O_2 reduction on a LSM cathode in the presence of a Fe–Cr alloy interconnect, measured under a cathodic current passage of 200 mA cm^{-2} at 900 °C

Cr at the $La_{0.6}Sr_{0.4}Co_{0.2}Fe_{0.8}O_3$ (LSCF) cathode/SDC electrolyte interface is very small as compared with that at the LSM/YSZ interface [132]. The mechanism of Cr deposition is considered to be controlled by an electrochemical reduction of high valent vapor species of chromium (CrO_3 and $Cr(OH)_2O_2$) to solid phase Cr_2O_3 in competition with the O_2 reduction reaction, followed by the chemical reaction of Cr_2O_3 with LSM to form $(Cr,Mn)_3O_4$ phases at the TPB, blocking the active sites [128–131, 133, 134]. The process can be written as follows [128]:

$$Cr(OH)_2O_2(g) + CrO_3(g) + 6e \rightarrow Cr_2O_3(s) + H_2O(g) + 3O^{2-}(YSZ) \quad (14)$$

$$3/2Cr_2O_3(s) + 3(La,Sr)MnO_3 \rightarrow 3(La,Sr)(Mn_xCr_{1-x})O_3 + (Cr_xMn_{1-x})_3O_4 + 1/4O_2 \quad (15)$$

$$3CrO_3(g) + 3(La,Sr)MnO_3 \rightarrow 3(La,Sr)(Mn_xCr_{1-x})O_3 + (Cr_xMn_{1-x})_3O_4 + 2.5O_2 \quad (16)$$

Jiang et al. [135–139] systematically investigated the interaction reaction between LSM cathode and Fe–Cr alloy interconnect and found that (a) Cr deposition on YSZ electrolyte occurs under cathodic as well as anodic polarization; (b) the initial polarization behavior is reversible, indicating no direct relation between the active sites for the O_2 reduction and the deposition of the Cr_2O_3 solid phase at the early stage of the reaction; (c) no preferential deposition of Cr at the TPB area, and (d) deposition of Cr occurs on the YSZ electrolyte surface far away from the LSM electrode that is not in direct contact with the alloy.

Figure 13 shows typical SEM micrographs of the YSZ electrolyte surface in contact with an LSM cathode in the presence of a Fe–Cr alloy at 900 °C after cathodic polarization at 200 mA cm^{-2} for different periods [139]. The LSM electrode coating was removed by a HCl treatment. Convex rings are the contact areas between LSM grains and the YSZ electrolyte surface, formed during the electrode sintering steps [140]. After cathodic current passage for 5 min, there is a formation of the isolated fine Cr grains at areas between the LSM particles (Fig. 13a). The density of the fine grains increases with the increase in the cathodic current passage time (Fig. 13b–f). However, the deposition of fine Cr grains is random, simply filling the space between the LSM particles with the increase in the cathodic polarization time. This shows that the deposition of Cr species is not controlled by electrochemical reduction of high-valent chromium species in competition with O_2 reduction at TPB. The driving force for the Cr deposition reaction is suggested to be related to the Mn^{2+} species generated under cathodic polarization or at high temperatures via the nucleation and grain growth steps [137, 139].

$$Mn^{2+} + CrO_3 \rightarrow Cr-Mn-O \text{ (nuclei)} \quad (17)$$

$$Cr-Mn-O \text{ (nuclei)} + CrO_3 \rightarrow Cr_2O_3 \quad (18)$$

$$Cr-Mn-O \text{ (nuclei)} + CrO_3 + Mn^{2+} \rightarrow (Cr,Mn)_3O_4 \quad (19)$$

The formation of $(Cr, Mn)_3O_4$-type spinel would be facile if there is sufficient supply of Mn^{2+} ions.

The interaction between the LSM/YSZ composite cathode and Fe–Cr alloy interconnect was also investigated under SOFC operation conditions [141]. Similar to the pure LSM electrode, no Cr species was observed on the surface of the LSM/YSZ composite electrodes. For LSM (10 wt.%)/YSZ (90 wt.%) composite cathode, there is significant deposition of Cr at the electrode/YSZ electrolyte interface, similar to that at the LSM electrode [137, 139]. In contrast to LSM and LSM (10 wt.%)/YSZ (90 wt.%) composite electrodes, the electrode/electrolyte interfaces are much cleaner in the case of LSM (30 wt.%)/YSZ (70 wt.%) and LSM (50 wt.%)/YSZ (50 wt.%) composite electrodes. This indicates the LSM/YSZ composite cathodes have a high tolerance and resistance toward Cr deposition.

The interaction between LSM coating and metallic interconnect has also been studied under open circuit conditions. Quadakkers et al. [142] studied transportation and deposition processes of Cr species on LSM, $LaCoO_3$, and Sr-doped $LaCoO_3$ (LSC) films coated on alumina-forming and chromia-forming alloys at 950 °C. In the case of chromia-forming alloy, Cr species were deposited over the whole width of the coating, forming spinel phases of $MnCr_2O_4$ for an LSM coating and $CoCr_2O_4$ for an LSC coating. Zhen et al. [143] recently studied the interaction between a Fe–Cr alloy interconnect and constituent oxides of LSM coating, La_2O_3, SrO, and Mn_2O_3.

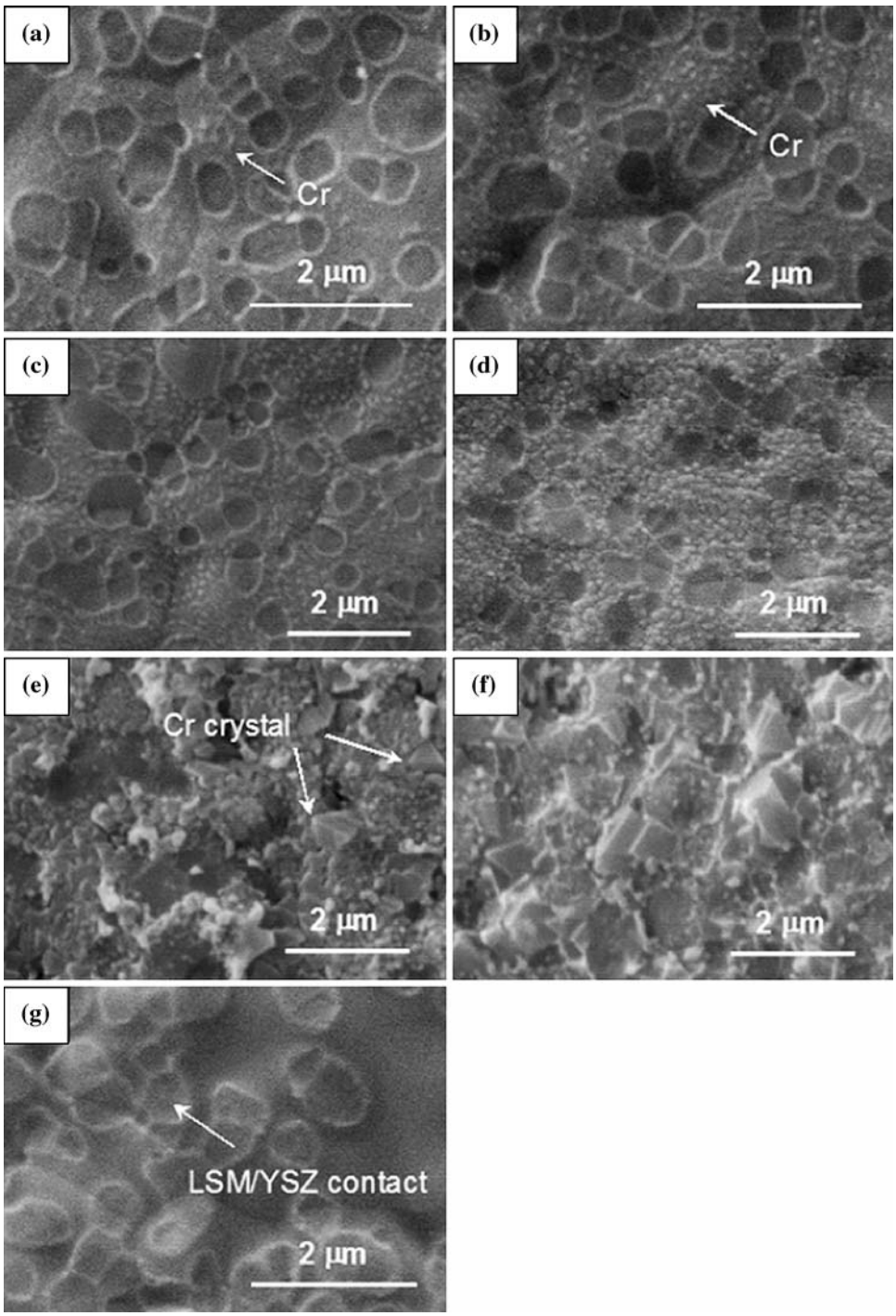

Fig. 13 SEM micrographs of the YSZ electrolyte surface in contact with a LSM cathode in the presence of a Fe–Cr alloy at 900 °C after cathodic polarization at 200 mA cm^{-2} for (**a**) 5 min, (**b**) 15 min, (**c**) 30 min, (**d**) 4 h, (**e**) 20 h, and (**f**) 50 h. The YSZ surface in contact with LSM electrode after polarization at 200 mA cm^{-2} at 900 °C for 4 h in the absence of Fe–Cr alloy is shown in (**g**) after Jiang et al. [139]. The LSM coating was removed by HCl treatment

The Cr deposition reaction between the Fe–Cr alloy and oxides varies significantly. The interaction between the Fe–Cr alloy and La_2O_3 and Mn_2O_3 oxides primarily results in the formation of $LaCrO_3$ and $(Cr, Mn)_3O_4$ while in the case of SrO oxide, Cr_2O_3 is the main product. The interaction between LSM-based coating and metallic interconnect is also studied by others for the potential application as the protective coating for metallic interconnect [144–148].

Interaction with other SOFC components

In addition to the YSZ electrolyte and metallic interconnect, SOFC stack also includes component materials such as seals and manifolds. Sealant materials based on glass or ceramic glass have been investigated to provide reliable seals between different SOFC components in the stack. In addition to the air tightness, the essential requirements for a sealant material are the chemical stability in oxidizing and

reducing atmospheres, low chemical activity to the cell components with which they come in contact, high insulating properties, matching thermal expansion coefficient, good wetting behavior, and stress relaxation ability during operation. It has been shown that loss of constitutes such as B_2O_3 in aluminosilicate glass [149] and commercial AF 45 glass [150] is detrimental to the durability of the material. However, the information between LSM cathodes and the seals and manifold materials is relatively rare. Jiang et al. [151] studied the effect of the gaseous species of the borosilicate glass system, A_2O–Al_2O_3–B_2O_3–SiO_2 (A = Na, K) on the microstructure and performance of LSM electrodes. There is a clear grain growth of LSM electrodes exposed to the glass containing Na or K. For example, the particle size of the LSM electrode exposed to the glass containing Na was 60% larger as compared to that in the absence of glass. This shows that in addition to the essential requirements in the softening, crystallization, and chemical stability of the sealant materials in SOFC, the constitutes in sealant materials should have low volatility to minimize the adverse effect on the performance and stability of SOFC stack components or the direct contact between the volatile species such as Na_2O and K_2O and the stack components such as LSM electrodes should be avoided through the stack design.

Polarization, activation, and degradation

Polarization-induced activation and microstructure change

LSM-based electrode shows a distinguished activation behavior under cathodic polarization or current passage [14, 152–155]. The activation behavior is characterized by a rapid decrease in the cathodic polarization potential and/or the electrode polarization (interface) resistance (R_E) after application of a cathodic polarization or current passage treatment, as shown in Fig. 14 [42]. For the O_2 reduction reaction on a freshly prepared LSM electrode, the initial polarization losses are very high and decrease significantly with the cathodic polarization/current passage (Fig. 14b). Consistent with the polarization potential, the impedance responses measured at open circuit decrease rapidly with the application of the cathodic current passage (Fig. 14a). Analysis of the impedance responses indicates that effect of the cathodic polarization is primarily on the reduction in the low-frequency impedance [14]. Clearly, the activation process is a very important phenomenon and is of great practical relevance as the electrode performance not only depends on the fabrication process (i.e., the microstructure), but also on the testing history [156].

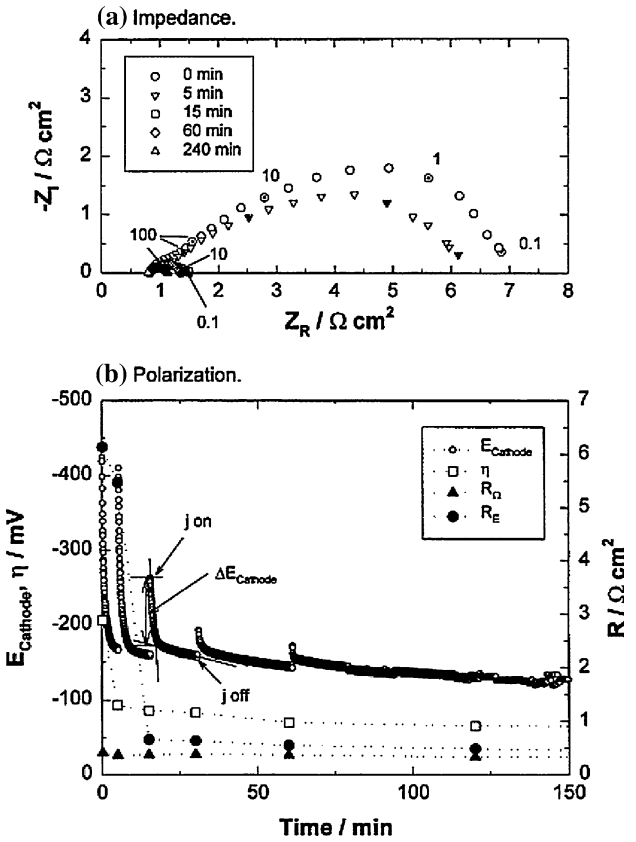

Fig. 14 Impedance (**a**) and polarization (**b**) behavior of a freshly prepared $La_{0.72}Sr_{0.18}MnO_3$ electrode for O_2 reduction as a function of cathodic polarization time at 200 mA cm^{-2} and 900 °C in air after Jiang and Love [42]. The impedance was measured at open circuit and the numbers are frequencies in Hz

Leng et al. [157] observed the activation effect of cathodic polarization/current passage on the polarization and impedance behavior of LSM (50 wt.%)/YSZ (50 wt.%) composite electrodes. Figure 15 shows the initial impedance responses of a stoichiometry $(La_{0.85}Sr_{0.15})_{1.0}MnO_3$/YSZ (LSM-A/YSZ) and a nonstoichiometry $(La_{0.85}Sr_{0.15})_{0.9}MnO_3$/YSZ (LSM-B/YSZ) composite cathodes as a function of cathodic current passage time at 200 mA cm^{-2} and 800 °C in air [157]. The size of the impedance arc decreases with the cathodic current passage time, indicating the activation effect of the cathodic polarization on the electrochemical activity of LSM/YSZ composite cathodes. However, the electrode interface resistance and the activation effect of the cathodic current treatment for the O_2 reduction on the A-site nonstoichiometry LSM-B/YSZ composite cathode are significantly smaller in magnitude as compared to that of the A-site stoichiometry LSM-A/YSZ composite cathode. The much higher electrode interface resistance for the reaction on LSM-A/YSZ composite cathode is probably due to the formation of a resistive phase between the stoichiometry LSM-A and YSZ [14]. The activation process of LSM/YSZ

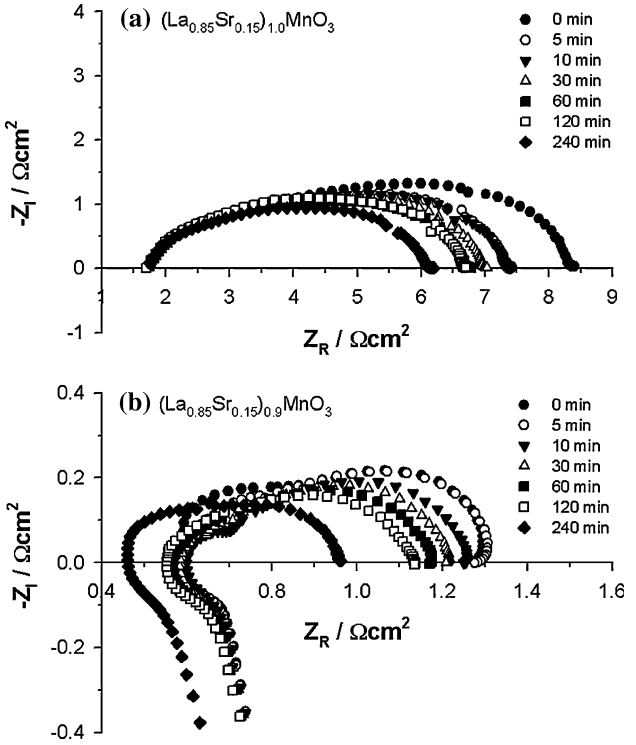

Fig. 15 Initial impedance responses of an A-site stoichiometry $(La_{0.85}Sr_{0.15})_{1.0}MnO_3$/YSZ (LSM-A/YSZ) and an A-site nonstoichiometry $(La_{0.85}Sr_{0.15})_{0.9}MnO_3$/YSZ (LSM-B/YSZ) composite cathodes as a function of cathodic current passage time at 200 mA cm^{-2} and 800 °C in air after Leng et al. [157]

composite cathodes is also reported by others [72, 158, 159]. Nevertheless, the activation effect of the cathodic polarization/current passage on LSM/YSZ composite cathodes appears to be much smaller than that on pure LSM electrodes (see Fig. 14).

The change in the microstructure under the influence of the polarization has been reported on the LSM-based cathodes by various research groups. Tsukuda and Yamashita [160] observed the microstructure change at the LSM/YSZ interface region after the cathodic current passage treatment. In a study of the impedance responses at the $La_{0.8}Sr_{0.2}MnO_3$ cathode/YSZ electrolyte interface, Kuznecov et al. [161] observed the formation of nanopores near the cathode/electrolyte interface after the aging of the LSM cathode at a dc voltage of 0.8 V for 3 h. Jiang and co-workers investigated in detail the effect of the polarization on the microstructure and the morphology of LSM electrodes [162, 163]. The microstructure of a freshly prepared LSM electrode is characterized by large agglomerates with no clear boundaries between LSM grains. After polarization treatments (e.g., cathodic or anodic polarization), large agglomerates disappear and change to much smaller and well-defined granular-shaped particles with clear boundaries. The morphology change caused by the cathodic current passage treatment cannot be reversed by a subsequent current passage treatment. Such a microstructural change occurs on the electrode surface as well as at the electrode/electrolyte interface. This indicates that the microstructure change under polarization is not due to the local heating as suggested by Tsukuda and Yamashita [160]. The microstructural change under polarization was also observed for the A-site stoichiometry LSM [153].

Polarization not only influences the microstructure change of the LSM electrode but also causes a morphological change at the interface between the LSM cathode and YSZ electrolyte. An atomic force microscopy (AFM) study of the YSZ electrolyte surface in contact with a LSM electrode before and after polarization treatments clearly show the interfacial change, as shown in Fig. 16 [140]. After removing the LSM electrode coating by HCl treatment, convex rings or dents approximately 0.5–1.0 μm in diameter can clearly be seen on the YSZ surface (Fig. 16a). The rings have sharp boundaries and a depth in the range of 90–140 nm. After the polarization treatments, the sharp edge of the convex rings disappears and the rings grow outwards. The average ring width is 0.15 ± 0.05 μm. Such interfacial changes induced by the cathodic polarization are not reversible under subsequent anodic polarization (Fig. 16c). Moreover, the anodic current treatment on a freshly prepared LSM electrode also induced a change in LSM/YSZ interface topography similar to the cathodic current treatment (Fig. 16d). This indicates that the initial LSM/YSZ interface formed by the thermal treatment of the system is morphologically unstable. The formation of convex rings on the YSZ electrolyte surface and their subsequent broadening under polarization indicate that oxygen reduction and oxidation reactions most likely occur at the O_2/LSM/YSZ TPB region.

Jiang and Love [42] provided some insight in the activation behavior by studying the electrochemical behavior of acid-etched LSM electrodes. In this experiment, an as-prepared $La_{0.72}Sr_{0.18}MnO_3$ electrode was treated with a 1 M HCl solution prior to the cathodic polarization. Figure 17 shows the initial impedance curves of an acid etched LSM under a cathodic current of 200 mA cm^{-2} at 900 °C in air [42]. The initial electrode polarization behavior of the acid-etched LSM is distinctively different from that of the LSM electrode without acid etching. The initial electrode polarization resistance, R_E, is significantly smaller and the reduction of R_E under the cathodic polarization treatment is also much smaller. This demonstrates that the activation process for the O_2 reduction on acid-etched LSM is not as effective as that without acid etching treatment. The ICP-AES analysis of the solution collected after the HCl etching of the LSM electrode coating shows that the concentration of Sr and Mn is one order of magnitude higher than that of La, indicating the Sr enrichment

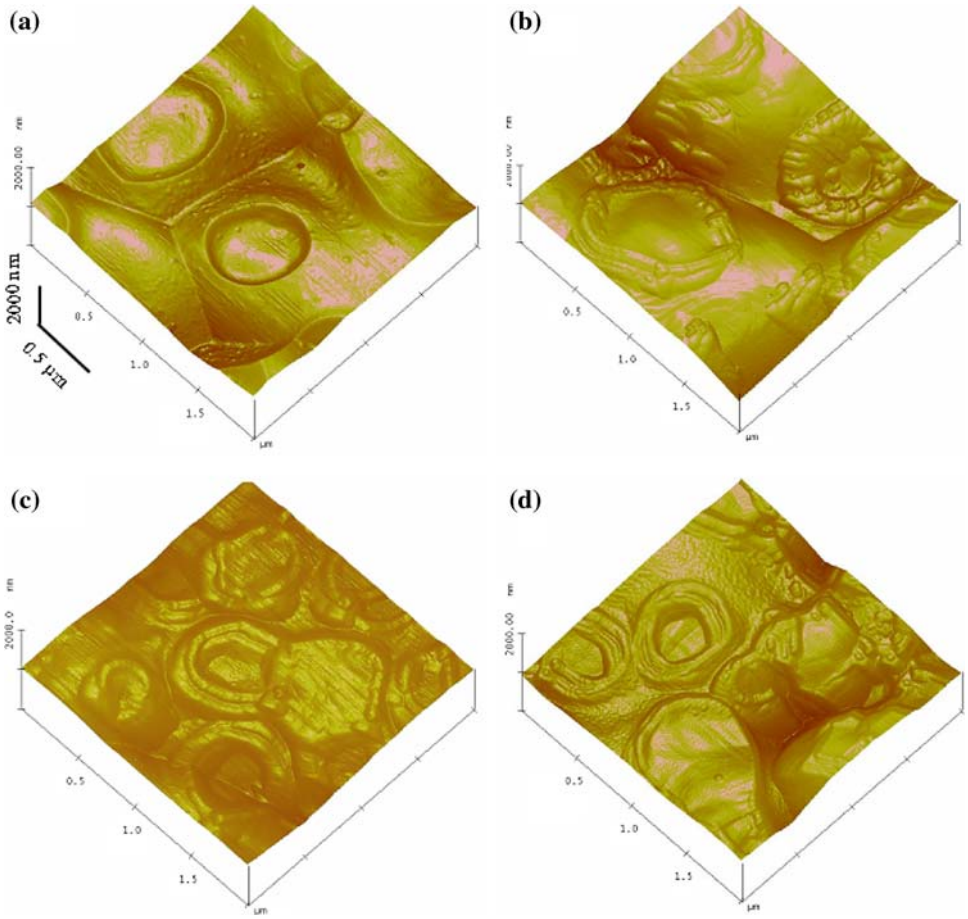

Fig. 16 AFM images of the YSZ electrolyte surface in contact with the LSM electrode: (**a**) before polarization, (**b**) after cathodic current passage for 3 h, (**c**) cathodic and anodic current passage for 6 h, and (**d**) anodic current passage for 3 h. All polarization treatments were performed under a current of 200 mA cm^{-2} at 800 °C in air. The LSM electrode was removed by HCl treatment after Jiang and Wang [140]. The scale bar applies to all AFM micrographs

on the LSM surface [42]. Thus, removal of the SrO species by a chemical process such as acid etching can lead to the significant improvement of the initial polarization performance and to the significantly reduced activation effect of the cathodic polarization.

Further studies indicate that the initial significant reduction in the electrode interface resistance and overpotential for the O_2 reduction reaction on freshly prepared LSM electrodes might be due to the incorporation of passive species such as SrO into the LSM perovskite structure under the cathodic polarization/current passage treatment [41]. The incorporation of SrO would be kinetically favorable due to the existence of the cation vacancies at the A-site. On the other hand, formation of oxygen vacancies occurs under cathodic polarization conditions [38, 164, 165]. Horita et al. [79] observed the enhanced oxygen exchange at the LSM/YSZ interface under a cathodic polarization potential of 0.3 V at 700 °C using oxygen isotope labeling and SIMS techniques. This indicates that the O_2 reduction reaction on LSM electrodes could be activated and enhanced by two processes: the removal of SrO species and the formation of oxygen vacancies. The first step could be primarily responsible for the initial rapid improvement of the electrocatalytic activity of the LSM electrode under the cathodic polarization.

Polarization performance

LSM cathode

The impedance behavior for the O_2 reduction on LSM-based cathodes is generally characterized by two depressed arcs and has been analyzed using equivalent circuits [152, 166]. Jiang et al. [90, 167, 168] studied in detail the electrode behavior of LSM cathodes over the temperature range of 850–1000 °C and oxygen partial pressure of 0.01–0.21 atm. Figure 18 shows the typical impedance responses for the oxygen reduction on a LSM cathode measured at 900 and 850 °C at different partial pressure of oxygen [168]. The impedance arc changes significantly with the temperature and partial pressure of oxygen, and is characterized by two separable arcs at low and high frequencies. The electrode process associated with the high-frequency arc is essentially independent of O_2 partial pressure with an activation energy of $\sim$74 kJ mol^{-1} while that at the low-frequency arc has an activation energy of $\sim$202 kJ mol^{-1} and has a reaction

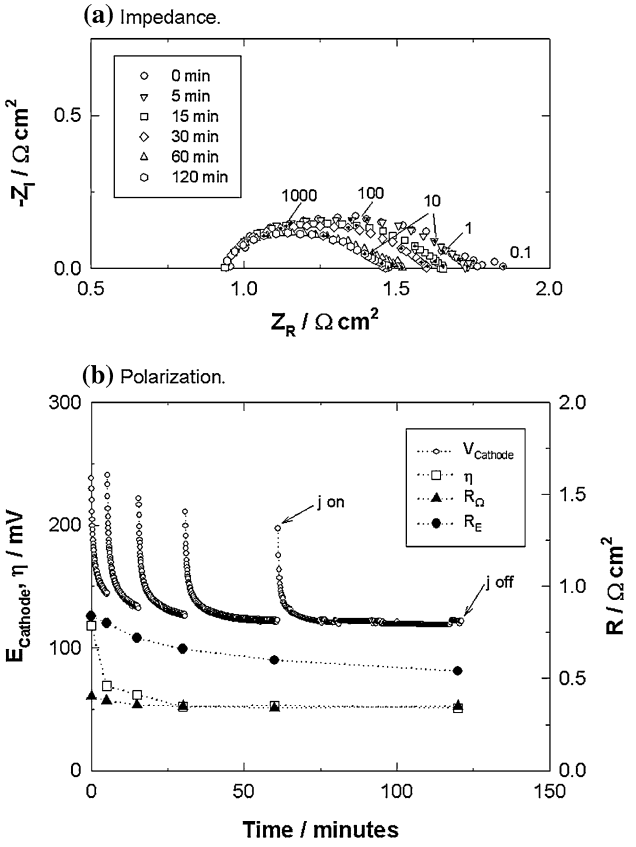

Fig. 17 Initial impedance curves of the 1 M HCl-etched LSM under a cathodic current of 200 mA cm^{-2} at 900 °C in air after Jiang and Love [42]. The numbers are frequencies in Hz

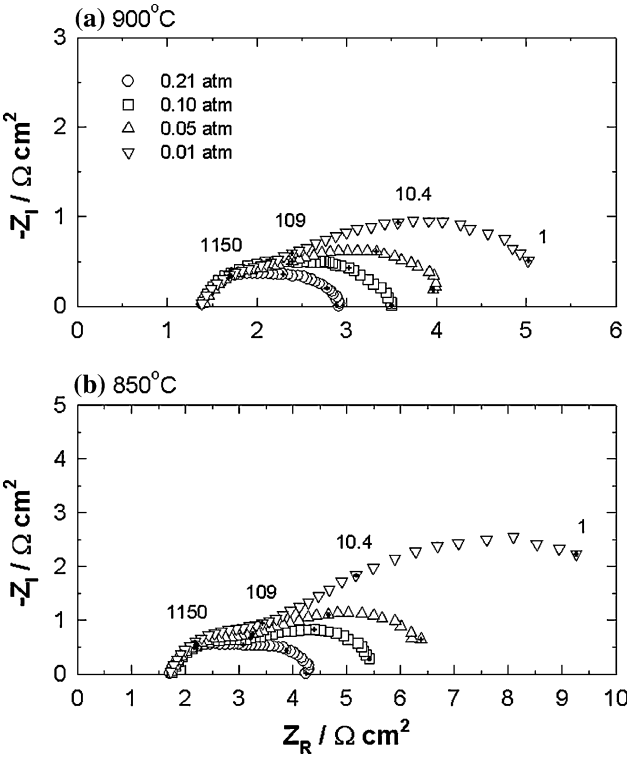

Fig. 18 Typical impedance responses for the oxygen reduction on a LSM cathode measured at 900 and 850 °C at different partial pressure of oxygen after Jiang et al. [168]. The numbers are frequencies in Hz

order with respect to O_2 partial pressure of $\sim$0.5 at low temperatures and $\sim$0.85 at high temperatures. The O_2 reduction reaction is limited by the diffusion of oxygen species on the LSM surface and the migration of oxygen ions into YSZ electrolyte.

Figure 19 is the typical polarization curves for the O_2 reduction on a $La_{0.72}Sr_{0.18}MnO_3$ cathode in air at different temperatures [90]. LSM electrode shows very high polarization losses particularly as the temperature decreases. At 100 mA cm^{-2}, η is 41, 256, and 542 mV for the reaction on the LSM electrode at 900, 800, and 700 °C, respectively. The dramatic increase in η for the reaction on LSM electrodes at low temperatures indicate that pure LSM would not be applicable for SOFC operating at intermediate and low temperatures. Due to the inherently very low oxygen ion conductivity of LSM-based oxides (see Table 4), the TPB area is very important for the O_2 reduction reaction on LSM electrodes as shown by Mizusaki et al. [169], van Heuveln et al. [170], and Fukunaga et al. [171].

Sasaki et al. [172, 173] investigated the effect of morphology of LSM powders, the cathode thickness, and current collector on the polarization performance of LSM electrodes. LSM electrode prepared from the powders with narrow particle size distribution and small particle size shows low electrode ohmic resistance and low polarization. The polarization losses are also dependent on the sintering temperature and the cathode thickness. The best electrode performance was obtained with the LSM cathode sintered at 1100 °C and with an electrode thickness of 25 μm.

The electrochemical activity of LSM cathodes for the O_2 reduction reaction is related to the Sr doping. Lee [174] studied the electrode polarization resistance and electrical conductivity of Sr-doped $LaMnO_3$. R_E decreases with the increasing Sr content and the lowest R_E is obtained when the amount of Sr is 50 mol% (Fig. 20). The lowest R_E (or R_{ct}) is corresponding to the highest electrical conductivity of $La_{1-x}Sr_xMnO_3$ with $x = 0.5$ [49]. Takeda et al. [175, 176] studied the polarization performance of $La_{1-x}Sr_xMO_3$ (M = Cr, Mn, Fe, Co) electrodes sputtered on YSZ electrolyte at 800 °C in air. LSC electrodes show highest electrocatalytic activity for O_2 reduction. In LSM system, the best polarization performance was observed for $La_{0.5}Sr_{0.5}MnO_3$ and the activation energy for the reaction on the LSM electrodes is $\sim$180 kJ mol^{-1}.

Overpotentials of LSM-based perovskites also depend on the A-site cations. Ishihara et al. [177] investigated the oxygen reduction activities of $Ln_{0.6}Sr_{0.4}MnO_3$ (Ln is La, Pr, Nd, Sm, Gd, Yb, and Y). The electrodes were prepared by slurry coating, followed by firing at 950 °C for 10 min.

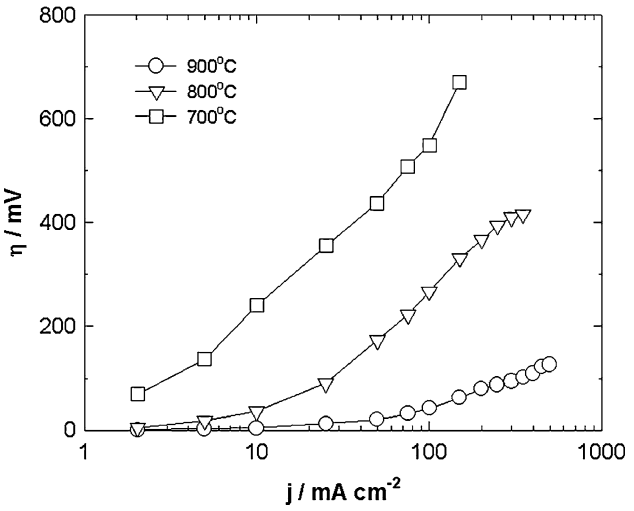

Fig. 19 Typical polarization curves for the O_2 reduction on a LSM cathode in air at different temperatures after Jiang [90]. LSM cathode was polarized at 200 mA cm^{-2} and 900 °C for 2 h before the measurements

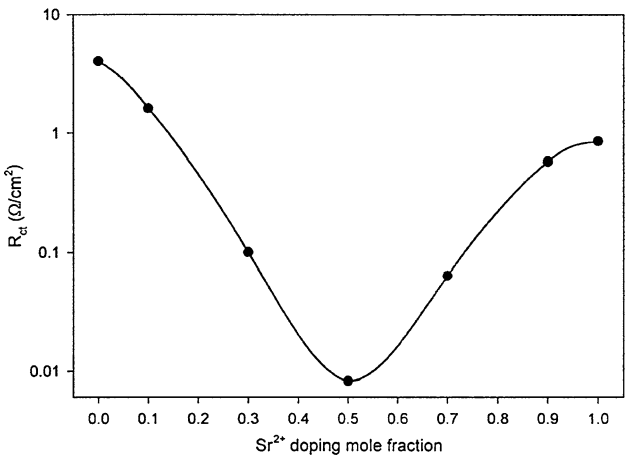

Fig. 20 Electrode polarization resistance (R_{ct} as shown in the figure) of $La_{1-x}Sr_xMnO_3$ cathode on YSZ electrolyte as a function of Sr doping at 1000 °C after Lee [174]

With Ln = La, Pr, Nd, Sm, and Gd, the conductivity is about 100–240 S cm^{-1} at 800 °C. For samples with Ln = Yb and Y, the electrical conductivity is between 35 and 50 S cm^{-1} at 800 °C. The overpotentials of the cathodes at 1000 °C decrease in the following order: Y > Yb > La > Gd > Nd > Sm > Pr.

The electrochemical activity of the electrodes follows similar order as the conductivity in respect to the Ln cations in $Ln_{0.6}Sr_{0.4}MnO_3$. This indicates the importance of the electronic conductivity for the cathodic activity of the materials. Further work established that (Pr,Sr)MnO_3 is far superior to (La,Sr)MnO_3 in terms of thermal expansion compatibility with YSZ electrolyte and electrochemical activity in the intermediate temperatures (Fig. 21) [178]. Praseodymium oxides exhibit nonstoichiometry in air.

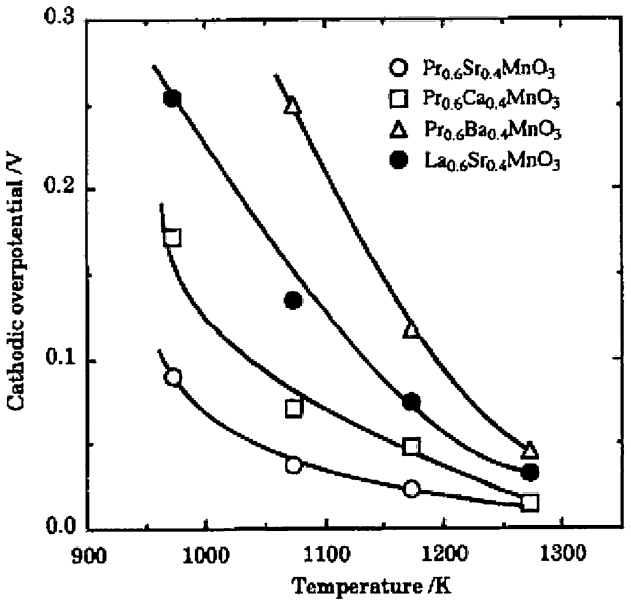

Fig. 21 Cathodic overpotential of some Mn-based perovskites at a current density of 0.1 A cm^{-2} as a function of test temperature after Ishihara et al. [178]

High activity of the $Pr_{0.6}Sr_{0.4}MnO_3$ could be attributed to the facile redox cycle of Pr ions. Huang et al. [179] also showed that A-site nonstoichiometry $Pr_{0.55}Sr_{0.4}MnO_3$ has significantly lower R_E than that of $Pr_{0.6}Sr_{0.4}MnO_3$ for the O_2 reduction at 850 °C.

Different results were reported by Sakaki et al. [60]. They studied the electrical conductivity and polarization performance of $Ln_{1-x}Sr_xMnO_3$ (Ln = Pr, Nd, Sm, and Gd; $0 \leq x \leq 0.5$) and found that the influence of the lanthanoid ions at the A-site on the electrical conductivity and electrocatalytic activity is not significant. Nevertheless, $Ln_{0.7}Sr_{0.3}MnO_3$ with Ln = Pr, Nd was suggested to be the suitable candidate cathodes for co-firing process due to their low reactivity with YSZ electrolyte.

LSM-based composite cathodes

Due to the high activation energy of the O_2 reduction reaction and negligible oxygen ionic conductivity of LSM-based electrodes, polarization resistance for the reaction on the LSM-based cathodes increases dramatically with the decrease of the SOFC operation temperature. For example, for the O_2 reduction on a LSM electrode, R_E is 0.39 Ωcm^2 at 900 °C and increases dramatically to 55.7 Ωcm^2 at 700 °C [167].

Various strategies have been developed to improve the electrocatalytic activities of LSM-based cathodes. One commonly used method is to introduce ionic conducting secondary phase such as YSZ and GDC to form a composite cathode [72, 99, 107, 180–188]. It has been shown that the R_E values can be reduced to a quarter of its original

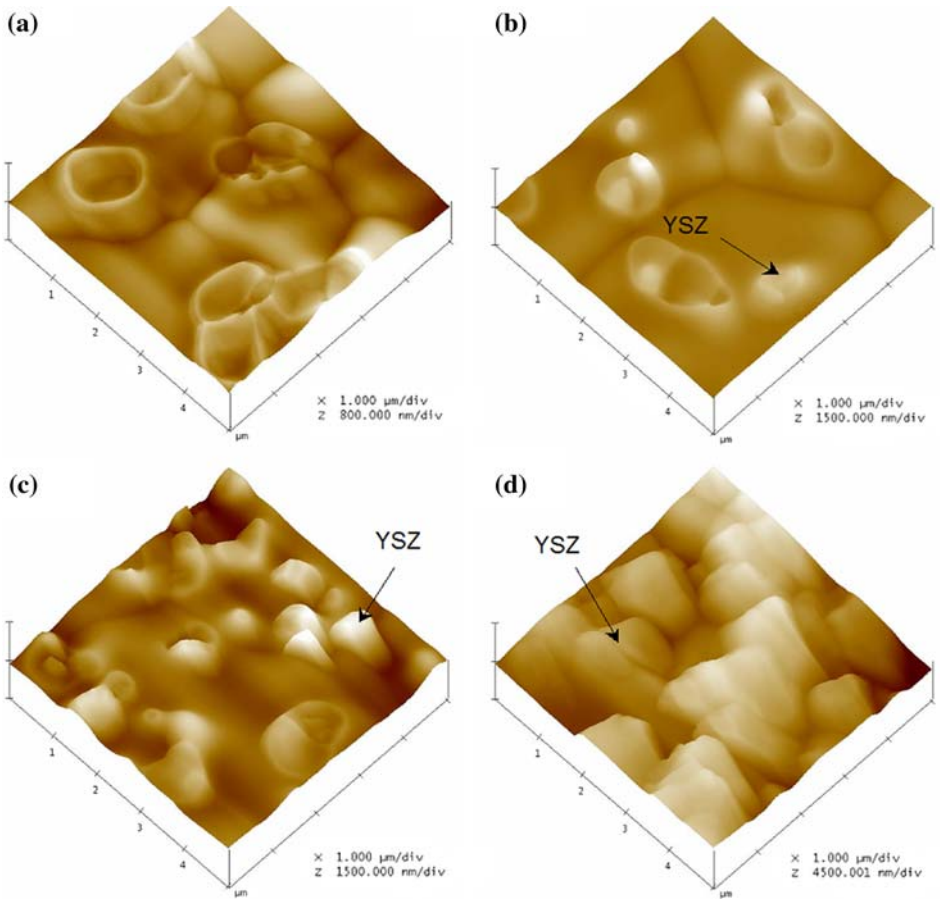

Fig. 22 AFM images of the YSZ electrolyte surface in contact with (**a**) LSM, (**b**) 90 wt.% LSM/10 wt.% YSZ, (**c**) 70 wt.% LSM/30 wt.% YSZ, and (**d**) 50 wt.% LSM/50 wt.% YSZ composite cathodes after Zhen and Jiang [187]. The LSM was removed by HCl treatment

value by adding 50 wt.% YSZ to a LSM cathode [107, 189]. The addition of YSZ phase reduces the grain growth of LSM by the intervening YSZ phase and significantly extends the TPB areas. Figure 22 shows the AFM images of the YSZ electrolyte surface in contact with LSM/YSZ composite cathodes after the removal of LSM by HCl treatment [187]. On the YSZ electrolyte surface in contact with the LSM/YSZ composite electrode, isolated white YSZ particles are formed and the number of YSZ particles on the YSZ electrolyte surface increases with the increase in the YSZ content in the composite electrodes (see Fig. 22b, c). As the YSZ content increases to 50 wt.%, interconnected YSZ particles are observed on the YSZ electrolyte surface (Fig. 22d). This indicates the formation of a three-dimensional network of YSZ phase in the 50 wt.% LSM/50 wt.% YSZ composite. The formation of YSZ network is also confirmed by the SEM examination of the acid-leached LSM/YSZ and LSM/Sc-doped YSZ composite electrodes [81]. The addition of YSZ can also reduce the risk of the formation of resistive $La_2Zr_2O_7$ phase which could be otherwise formed at the electrode/electrolyte interface, enhancing the electrode activity [107].

Similar to that of the LSM cathode, the performance of LSM-based composite cathodes is also strongly related to the microstructure. Jorgensen et al. [183] studied the effect of sintering temperature on the microstructure and performance of LSM/YSZ composite cathodes. R_E value of the composite cathode sintered at 1150 °C is 0.03 Ωcm^2 at 1000 °C, significantly lower than 0.11 Ωcm^2 for the composite cathode sintered at 1300 °C. The higher R_E for the LSM/YSZ composite cathode sintered at 1300 °C is due to the denser structure and larger grain size of the composite. Among the LSM/YSZ composite cathodes sintered between 1000 and 1300 °C, Choi et al. [182] reported the lowest polarization losses for the LSM/YSZ composite cathodes sintered at 1100 °C. Jorgensen et al. [183] also showed that microstructure of the current collector on the cathode side plays an important role in the electrochemical activities of LSM/YSZ composite cathodes.

The starting particulate materials have significant effect on the microstructure and performance of LSM and LSM composite cathodes. In particular, the composite cathode involves at least two or more different materials in which constituents may differ in their densification behavior. Song et al. [190] studied the cathodic performance of LSM/YSZ composite cathodes using fine (~81 nm) and coarse (~210 nm) LSM powders and the results show that the use of fine LSM powders induces extensive grain

growth, leading to the reduction in TPB and thus the increase in the polarization losses. This indicates that the use of nano-scale LSM materials may allow enhancement of the TPB due to the increased particle-to-particle contact points. However, the difference in the sinterability between phases could prevent the development of the effective three-dimensionally interconnected composite structure because of the excess densification of the highly sinterable and fine LSM phase. Thus, the control of the LSM and YSZ particle sizes and processing conditions is critical to achieve the best performance of the composite cathodes.

Murray and Barnett [191] reported that 50 wt.% addition of GDC instead of YSZ reduces the R_E to 1.06 Ωcm^2 at 700 °C and 0.49 Ωcm^2 at 750 °C, which is two to three times lower than for LSM/YSZ composite on YSZ electrolyte. Figure 23 shows the electrode polarization resistance of a LSM/GDC composite cathode tested in air [191]. R_E decreases as the GDC concentration increases to 50 wt.%. The rapid increase of the R_E value with further increase in GDC content above 50 wt.% may be due to a decrease in electrical conductivity. Xia et al. [181] studied the LSM/GDC composite cathodes fabricated by the sol–gel process. The sol–gel-derived composite cathodes show an electrode polarization resistance, 0.16 Ωcm^2 at 750 °C, lower than that obtained by the slurry coating technique [192]. LSM/$Ce_{0.7}Bi_{0.3}O_2$ (LSM/BDC) composite electrode also shows a reasonable electrochemical activity for the O_2 reduction at intermediate temperatures (R_E is 1.78 Ωcm^2 at 700 °C) [193].

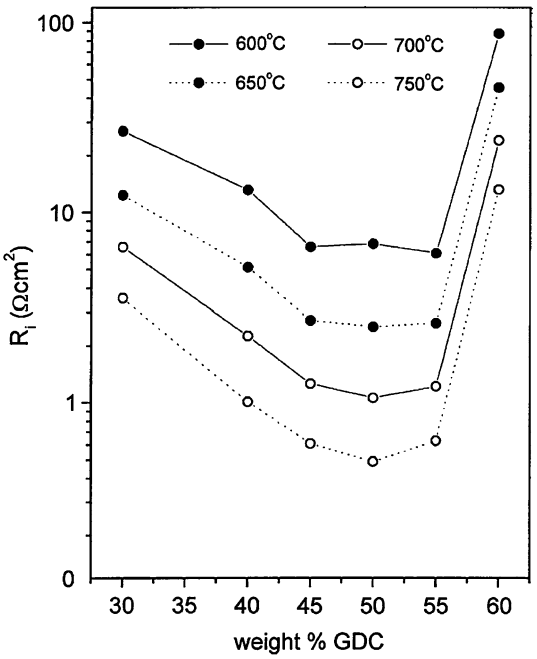

Fig. 23 Plots of electrode polarization resistance versus the GDC content in the LSM/GDC composite cathodes at different temperatures after Murray and Barnett [191]

Yi and Choi [194] studied the $La_{0.9}Sr_{0.1}MnO_3$/$La_{0.9}Sr_{0.1}Ga_{0.8}Mg_{0.2}O_3$ (LSM/LSGM) composite cathodes and the LSM/LSGM composite cathodes showed smaller particle size and lower overpotential than that for the LSM cathode. Armstrong and Virkar [195] studied the performance of anode-supported YSZ thin electrolyte cells with LSM/LSGM composite cathodes. In the composition range, 30–70 wt.% LSGM in the composites, the cathode overpotential varies between 65 and 400 mV at 1.0 A cm^{-2} at 800 °C and exhibits a minimum for the 50/50 composition. The cell with the 50/50 composition cathode interlayer achieved the best performance with a maximum power density of 1.4 W cm^{-2} at 800 °C. It was suggested that the sintering temperature of the LSM/LSGM composite cathode interlayer on YSZ electrolyte should be lower than 1200 °C to avoid the phase reaction between LSGM and YSZ. On the other hand, Pena-Martinez et al. [196] showed that the electrode polarization resistance and overpotential for the O_2 reduction on a LSM/LSGM composite cathode are substantially higher than that of LSM cathode. SEM analysis indicates that LSM cathode is more porous and uniform as compared to that of the LSM/LSGM composite cathode. This indicates that the microstructure is important for the polarization performance of the composite electrode.

The electrochemical performance of LSM cathode can also be enhanced substantially by introducing catalytic active nanoparticles, such as doped CeO_2, into the LSM porous structure. Tanner et al. [197] demonstrated theoretically that nano-structured electrodes with significantly higher surface area offer superior electrochemical properties, as long as a sufficiently large pore size and enough porosity are provided. This is supported by the dramatically reduced electrode/electrolyte interfacial polarization resistance and improved cell performance of nano-structured electrodes prepared by a combustion CVD process [198].

Wet impregnation is probably one of the most effective methods to introduce the nano-sized particles into porous electrodes of SOFCs [199]. Microstructure of the impregnated electrode is characterized by a uniform distribution of very fine and well-dispersed oxide particles in a porous electrode backbone. Jiang and Wang [200, 201] studied in detail the microstructure and electrochemical behavior of $Gd_{0.1}Ce_{0.9}O_3$-impregnated LSM cathodes. For a pure LSM electrode, LSM grains are in the range of 0.7–1.2 μm. After the wet impregnation with $Gd_{0.1}Ce_{0.9}(NO_3)_x$ solution, very fine particles are formed around LSM particles and their particle size is in the range of 100–200 nm. In the case of a 5.8 mg cm^{-2} GDC-impregnated LSM electrode, R_E is 0.21 Ω cm^2 at 700 °C, which is 56 times smaller than 11.7 Ω cm^2 measured on a pure LSM cathode at the same temperature. The R_E value of the 5.8 mg cm^{-2} GDC-impregnated LSM electrode is much lower than that of conventional LSM/YSZ and LSM/GDC composite

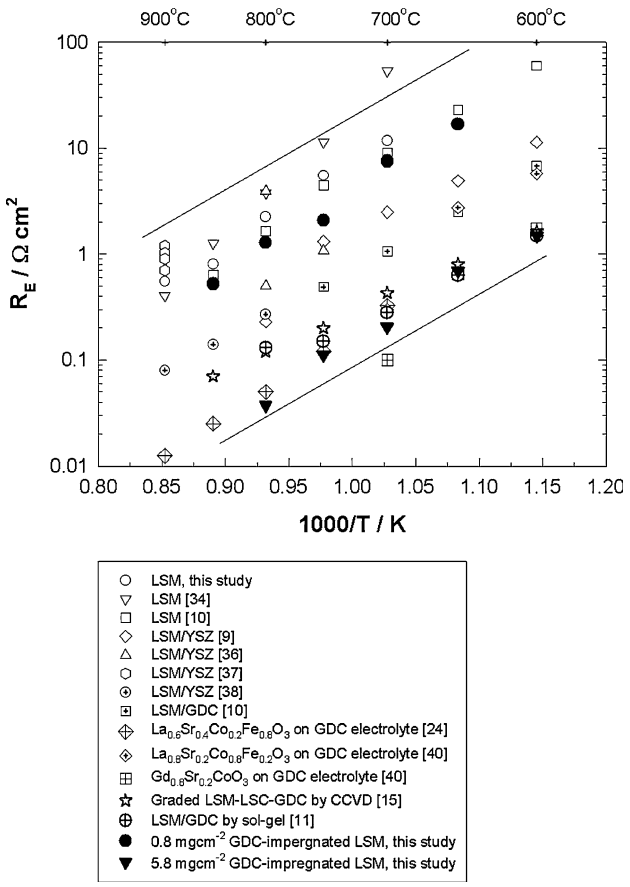

Fig. 24 A comparison of the electrode polarization resistance (R_E) of GDC-impregnated LSM electrodes with those of pure LSM, LSM/YSZ, LSM/GDC, and selected MIEC electrodes after Jiang and Wang [201]. Numbers are the references cited in [201] and lines are for guidance only

cathodes and is also close to that of the well-known mixed ionic and electronic conducting cathodes such as LSCF and $Gd_{0.8}Sr_{0.2}CoO_3$ (see Fig. 24) [201]. Yamahara et al. [202] examined the performance of anode-supported scandia-stabilized zirconia (SYSZ) thin-film cells with LSM/SYSZ composite cathodes impregnated with cobalt nitrate solution. Cobalt infiltration improves the peak power densities by as much as a factor of 1.8 at 650 °C. This indicates that through the proper composition optimization and materials engineering of the electrode structure, LSM-based electrodes can be used for ITSOFCs.

Cathode not only functions as the sites for electrochemical reaction but also the conductor to electrical current. The former is related to the regions associated with the interface to the solid electrolyte while the later is related to the current collector layer. Juhl et al. [203] showed that double-layer cathode made with LSM and YSZ in the electrochemically active layer improves the electrochemical performance of the cathode. Thus, in principle, a cathode composed of a number of individual layers with different functionality and characteristics should be advantageous as compared to single layer structure [198, 204, 205]. However, multi-layer structure requires repeated production steps and this could increase the cost of the cell production.

LSM cathodes in single-chamber SOFC

Single-chamber SOFC or SC-SOFC operates under a unique mixture of hydrocarbon fuel and air [206]. Good performance as well as reasonable open circuit potential can be achieved through the catalytic properties of the electrode materials against the hydrocarbon/oxygen mixture that provide for the build-up of proper P_{O_2} difference over anodes and cathodes. The anode must be as much as possible selective toward the partial oxidation of hydrocarbons. On the contrary, the cathode must be as much as possible inert toward the oxidation of hydrocarbons and only active to the oxygen reduction reaction.

The catalytic activity and performance of LSM and LSM/YSZ composite have been investigated as cathodes in SC-SOFC. Morel et al. [207] reported that the catalytic activity of LSM cathode depends significantly on the morphology and microstructure of LSM, e.g., LSM coating sintered at 1100 °C is much more active toward CH_4 conversion than the LSM sintered at 1200 °C. This is due to the fact that the particle size of LSM sintered at 1200 °C is significantly larger than that sintered at 1100 °C. The cell tested at 600 °C (the actual cell temperature is 678 °C) shows a significantly higher performance compared to a cell running at 700 °C (the actual cell temperature is 770 °C). The reduced cell performance was suggested to be due to the increased catalytic combustion at 700 °C, leading to the increased oxygen conversion and thus the reduced open circuit potential (OCP). The limits of the upper operating temperature of SC-SOFC with LSM cathodes on the basis of OCP have also been suggested by Demin and Gulbis [208].

Factors affecting the polarization performance of LSM-based cathodes

In addition to the effect of the cathodic polarization, composition, microstructure on the LSM electrode behavior as discussed above, the polarization performance of LSM cathodes is also affected by factors such as the cell size, the contacts between the electrolyte and LSM electrode and between the current collector and LSM electrode, the mechanical loading, the electrode thickness, etc. The processing–microstructure–property relations are important for the design and tailoring of the LSM-based cathode for SOFC.

Sasaki et al. [172, 173] investigated the effect of current collector on the polarization performance of LSM electrodes. Both the cathodic polarization and the ohmic loss

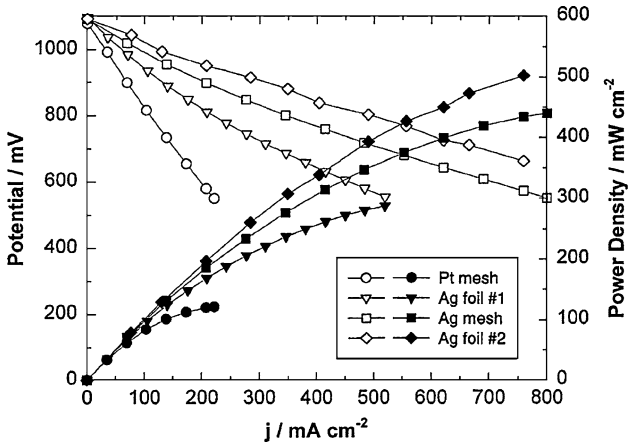

Fig. 25 Performance curves of 50 mm × 50 mm anode-supported cells measured under 97%H_2/3%H_2O fuel and air at 800 °C with different current collectors on the $Pr_{0.8}Sr_{0.2}MnO_3$ cathode side after Jiang et al. [53]. The contact area of Pt mesh, Ag foil #1, Ag mesh, and Ag foil #2 was 4.62, 9.50, 13.48, and 27.2%, respectively

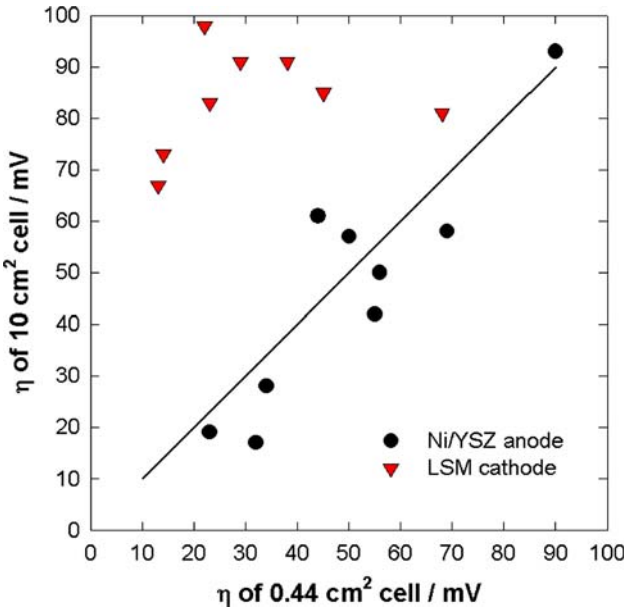

Fig. 26 The performance of LSM cathodes and Ni/TZ3Y cermet anodes obtained on small button cells and on 50 mm × 50 mm plate cells at 900 °C in air and in 97%H_2/3%H_2O, respectively, after Jiang [212]. The overpotentials were measured at 250 mA cm^{-2} and 900 °C. The effective electrode area of small coupon cells was 0.44 cm^2 and for 50 mm × 50 mm plate cells the effective electrode area was 10 cm^2. The small coupon cells and 50 mm × 50 mm plate cells were fabricated at the same time using the same LSM and Ni/TZ3Y inks

increase considerably with the increasing contact spacing, i.e., the decrease in the contact areas between the current collector and the LSM coating. The increased electrode ohmic resistance is often called constriction resistance or residual resistance [209, 210]. Similar phenomenon was also observed by Jiang et al. [53]. Figure 25 shows the performance curves of 50 mm × 50 mm anode-supported cells measured under 97%H_2/3%H_2O fuel and air at 800 °C with different current collectors on the $Pr_{0.8}Sr_{0.2}MnO_3$ cathode side [53]. In the cells tested, electrode and electrolyte materials are identical and the only significant difference is the current collector used on the cathode side; therefore, the difference in the cell performance is mainly related to the contact areas between the cathode and the current collector. Analysis of the results showed that both cell resistance and cell overpotentials decreased significantly with the increase in the contact area. Significant reduction in cell resistance and polarization losses is also reported by Itagaki et al. on metal wire mesh current collector electrophoretically coated with LSM [211].

Polarization performance of LSM electrodes is also found to be dependent on the cell size [212]. Figure 26 shows the performance of LSM cathodes and Ni/TZ3Y cermet anodes measured on small button cells and on 50 mm × 50 mm plate cells at 900 °C and 250 mA cm^{-2} in air and in 97%H_2/3%H_2O. For Ni/TZ3Y cermet anodes, there is a very good correlation between the performance measured on small button cells and on 50 mm × 50 mm cells. For LSM electrodes, the performance measured on 50 mm × 50 mm plate cells is significantly lower than that measured on small button cells, in most cases. This indicates that the size of the cell has significant effect on the performance of LSM cathodes. Thus the current collector design on the LSM cathode side is particularly important for the performance of a SOFC stack.

The contact resistance between the LSM electrode coating and current collector is also affected by the mechanical loading to the cell [212], see Fig. 27. Contact resistances on 50 mm × 50 mm cells are measured between a conventional voltage probe and a special voltage probe on the same electrode side using a special cell configuration [213]. The contact resistance decreases significantly with increase in the mechanical loading. The high contact resistance results in high polarization losses as the constriction effect not only occurs at the electrode/electrolyte interface but also at the interface between the electrode and current collector contact [53]. The electrical conductivity measurement on the porous electrode coatings showed that electrical conductivity of the porous Ni/TZ3Y cermet coating was ~254 S cm^{-1}, which is much higher than 45 S cm^{-1} for the porous LSM electrode coating at 800 °C [53]. The relatively lower electrical conductivity of porous LSM cathode coating may be the reason for the sensitivity of the polarization performance with the cell size and of the contact resistance with the mechanical load.

Performance of LSM cathode appears to be related to the ionic conductivity of the electrolyte or interface. Uchida et al. [214] carried out a detailed study on the effect of ionic conductivity of zirconia electrolytes on the polarization

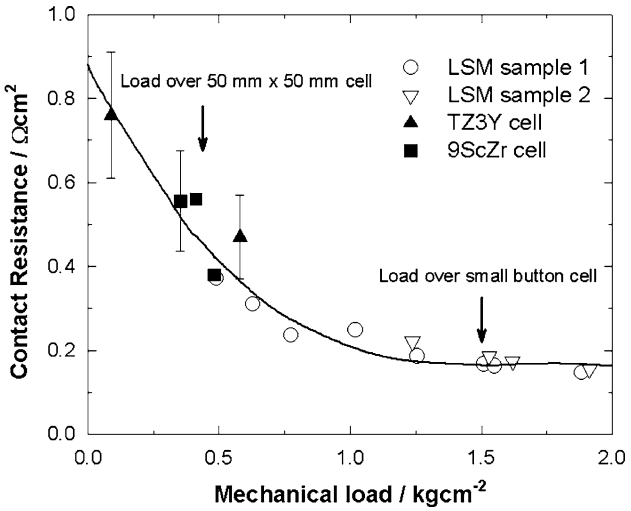

Fig. 27 Dependence of contact resistance between the LSM cathode and Pt mesh current collector on the mechanical loading measured at 800 °C after Jiang [212]. In the figure, the *open symbols* are the measured results of two different LSM electrode samples. The *solid triangles* are the LSM cathode side contact resistance measured on 50 mm × 50 mm TZ3Y electrolyte cells and the *solid squares* are the LSM cathode side contact resistance measured on 50 mm × 50 mm 9 mol% Sc_2O_3–ZrO_2 electrolyte cells

behavior of LSM. The electrochemical activity of LSM electrodes increases with the ionic conductivity of zirconia electrolytes in the temperature range of 800–1000 °C studied. Tsai and Barnett [215] studied the addition of Y_2O_3-doped CeO_2 (YDC) interlayers on both sides of the YSZ electrolyte on the performance of a cell with LSM cathode and Ni/YSZ anode. Adding thin porous YDC layers on the YSZ electrolyte surface significantly reduced the interfacial resistance, leading to the substantial improvement in the cell performance. The effect of YDC interlayer on the cathode side was suggested to promote the oxygen surface exchange coefficient. Increasing the roughness of the YSZ electrolyte by methods such as chemical treatment also increases the performance of LSM cathode [216].

The thickness of LSM coating may have limited effect on the electrochemical performance of the LSM cathodes but in the case of using LSM as cathode current collector, the thickness of the LSM coating is important. As shown by Lai and Barnett [217], the resistance of the segmented-in-series cells with relatively short cell length of 1.4 mm can be reduced by a factor of 2–3 when the LSM thickness increased from 11 to 91 μm.

Sintering properties and performance stability

Sintering behavior

In SOFCs, stability of electrode materials such as Sr-doped $LaMnO_3$ (LSM) and Ni/Y_2O_3-ZrO_2 (Ni/YSZ) cermet is a major concern for the long-term performance at SOFC operation temperatures [2]. The structural stability of an electrode is closely related to the sintering behavior of the electrode material. In the case of Ni/YSZ cermet electrodes, the sintering behavior is dominated by the agglomeration and grain growth of Ni particles and critically related to the content of Ni and YSZ phases in the cermet [218]. An agglomeration of Ni particles in the cermet can lead to a significant reduction in the TPB areas and to an increase in the electrode polarization resistance for the H_2 oxidation reaction [219]. Optimization of the phase distribution between Ni and YSZ is critical to inhibit agglomeration and sintering of Ni particles and to improve the performance stability of the anode [218, 220, 221].

Different to Ni/YSZ cermet anodes, defect chemistry plays a major role in the sinterability of LSM materials. It has been found that LSM with an A-site-deficient composition ($x < 1$) sinters more readily than their B-site-deficient counterparts ($x > 1$) [91, 222]. Berenov et al. [77] studied the sintering behavior of $LaMnO_3$ and $La_{0.9}MnO_3$ and found that the cation deficiency considerably improves the sinterability of the manganites and shifts the sintering curves to lower temperatures. Stevenson et al. [223] suggested that the densification of manganites is limited by the La diffusion. In SOFCs based on YSZ electrolyte, the A-site-deficient composition is often preferred to reduce the formation of resistive phases such as $La_2Zr_2O_7$ or $SrZrO_3$ at the interface between LSM and YSZ [14, 100]. On the other hand, Katayama et al. [224] and Hammouche et al. [9] suggested that the Mn^{4+} concentration determines the sintering behavior, although the exact mechanism was not elucidated. Poirson et al. [225] studied the sintering of $La_{0.8}Sr_{0.2}MnO_3$ by dilatometric measurement. Two sintering stages were identified. Below 1200 °C, the neck formation is the rate-limiting step while, above this temperature, the processes of grain growth dictates the sintering behavior of the materials.

Microstructural stability of LSM cathodes is found to be related to the thermal behavior of the cathode during the thermal cycling. Mori [226] studied the expansion and shrinkage of sintered $La_{0.8}Sr_{0.2}MnO_3$ during the thermal cycling in the temperature range between 600 and 1100 °C. Porous LSM samples with relative densities < 88% show shrinkage behavior during the thermal cycling and their densities increase gradually with increasing thermal cycling up to ~1,000 cycles. A decrease in pores in the LSM samples after thermal cycling has been observed by SEM analysis. The shrinkage of the LSM perovskite is considered to be caused by a change between the hexagonal and the tetragonal symmetries due to the release and absorption of oxygen.

Jorgensen et al. [227] investigated the performance and microstructure stability of LSM/YSZ composite cathodes

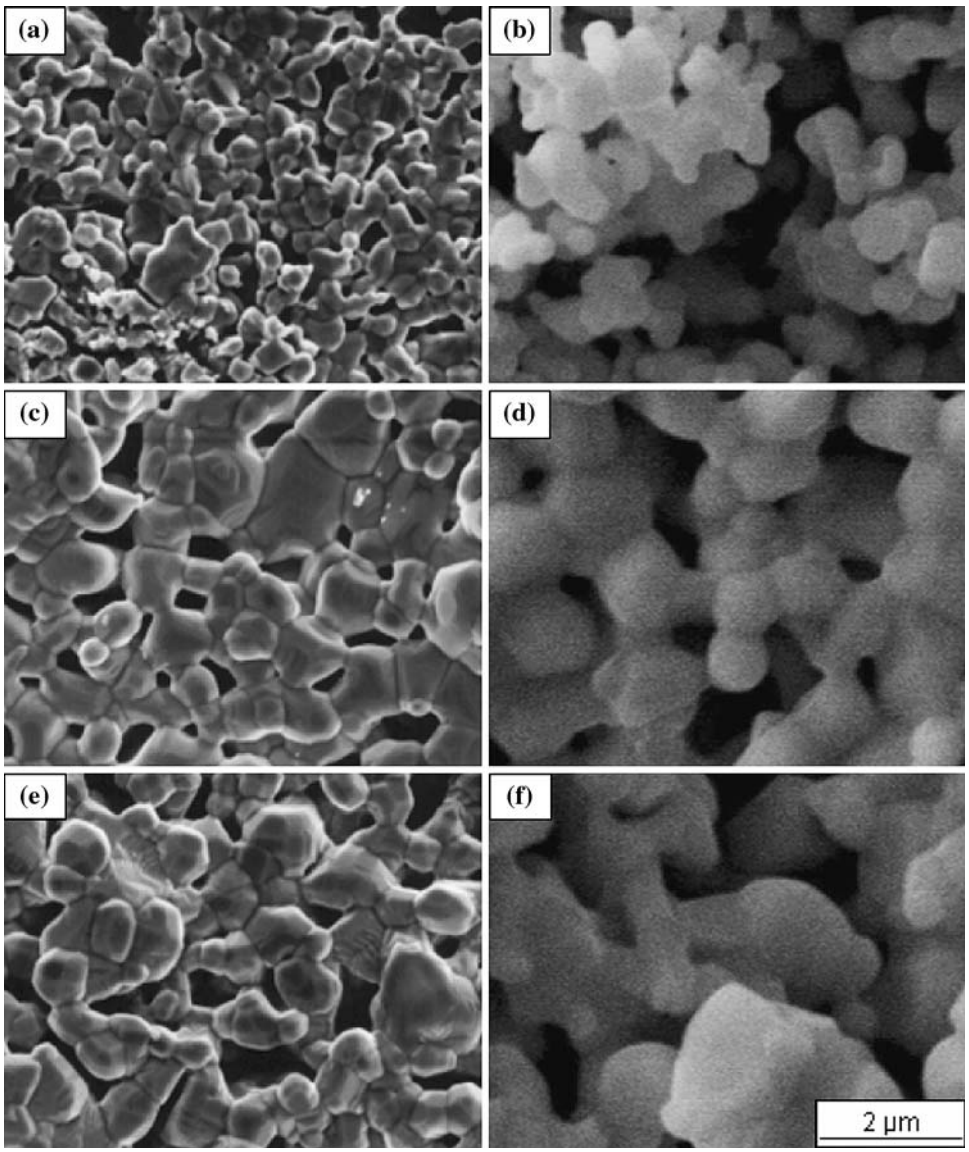

Fig. 28 SEM micrographs of the electrode surface of $(La_{0.8}Sr_{0.2})_xMnO_3$ with (**a**) $x = 1.0$, (**c**) $x = 0.9$, and (**e**) $x = 0.8$ sintered under a current load of 500 mA cm^{-2} and with (**b**) $x = 1.0$, (**d**) $x = 0.9$, and (**f**) $x = 0.8$ sintered under no current load at 1000 °C in air for 1600 h after Jiang and Wang [228]

under a cathodic current of 300 mA cm^{-2} at 1000 °C for 2000 h. The overpotential losses are doubled and there is an increase of the porosity at the composite electrode and the YSZ electrolyte interface. On the other hand, they did not observe such structural changes for the composite cathodes sintered under open circuit conditions. Wang and Jiang [162] studied the effect of polarization on the morphology of LSM materials and found that the morphology of LSM changes significantly under cathodic and anodic polarization. The change in the morphology of LSM particles is most likely related to the lattice expansion or shrinkage under either cathodic or anodic polarization.

To understand the structural and performance stability of LSM cathodes under SOFC operating conditions, Jiang and Wang [228] carried out a comparative study on the sintering behavior of $(La_{0.8}Sr_{0.2})_xMnO_3$ ($x = 1.0$, 0.9, 0.8) cathodes under polarization and open circuit conditions at 1000 °C for 1600 h. Figure 28 shows the SEM micrographs of the surface of LSM electrodes sintered at 1000 °C in air with and without a cathodic current passage of 500 mA cm^{-2} for 1600 h [228]. For the $(La_{0.8}Sr_{0.2})_{0.9}MnO_3$ electrode, particle size of the LSM grains is 0.88 ± 0.30 μm after sintering at 1000 °C under a current load of 500 mA cm^{-2} for 1600 h, significantly smaller than 1.17 ± 0.25 μm observed for the LSM coating sintered at open circuit under the same conditions (Fig. 28c, d). Similar trend was observed for the LSM electrodes with different compositions. The results indicate that the grain growth and sinterability of LSM electrode materials is reduced under cathodic polarization conditions as compared to those sintered under open circuit conditions. The driving force for the sintering process is the reduction of surface energy by the formation of large particles. This is most likely achieved by the cation diffusion at the A-site in the case of LSM materials [91, 223]. The

hindrance of sintering under cathodic polarization has been attributed to the elimination of cation vacancies at the A-site, thus increasing the sintering resistance of LSM cathodes [228].

Performance stability and degradation

Generally speaking, the literature in long-term stability and degradation behavior of SOFC electrodes is not plentiful probably due to the high cost of conducting long-term testing. However, the long-term stability is a major concern in the development of SOFC technologies and has been tackled primarily by SOFC industrial developers. It has been shown that SOFC stack with LSM-based cathode is stable under SOFC operating conditions [229–231]. For example, Singhal [231] reported the long-term stability of a tubular cell with a doped $LaMnO_3$ cathode over 69,000 h at 1000 °C with a cell degradation rate of less than 0.5% per 1000 h.

Figure 29 shows the polarization stability of LSM cathodes for the O_2 reduction reaction under a constant current load of 500 mA cm^{-2} at 1000 °C for 1600 h [228]. The initial high polarization losses indicate the activation effect of the cathodic polarization on LSM electrodes. In the composition range studied, LSM electrodes showed no degradation over the period studied. Nevertheless, the interface between the cathode and electrolyte undergoes significant changes under SOFC operating conditions. Figure 30 is the SEM micrograph of a $La_{0.72}Sr_{0.18}MnO_3$ cathode after a long-term stability test under a current density of 250 mA cm^{-2} and air at 1000 °C for 2543 h [228]. Two features can be seen from the cross section of the electrode after the long-term polarization test. Isolated dark particles with high Mn content appear in the electrode. This indicates the formation of Mn-rich, probably Mn_3O_4,

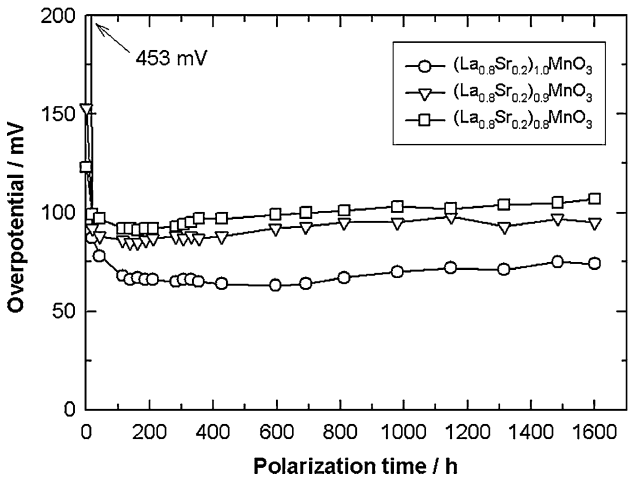

Fig. 29 Polarization stability of LSM cathodes for the O_2 reduction reaction under a constant current load of 500 mA cm^{-2} at 1000 °C for 1600 h after Jiang and Wang [228]

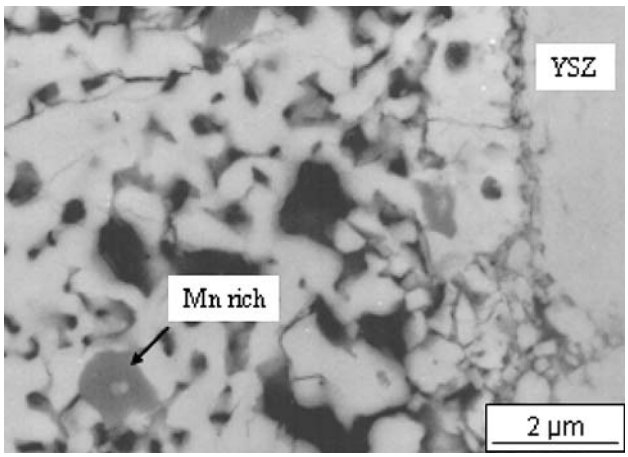

Fig. 30 SEM micrograph of the cross section of a LSM electrode after the fuel cell testing on a 50 mm × 50 mm cell with Ni (50 vol.%)/YSZ (50 vol.%) anode under a current density of 250 mA cm^{-2} in 96%H_2/4%H_2O and air at 1000 °C for 2543 h after Jiang and Wang [228]

phase inside the LSM electrode after the cathodic polarization. The formation of Mn-rich region in the LSM electrode is most likely due to the significant diffusion and migration of manganese species under the cathodic polarization conditions. The second feature is the appearance of voids at the LSM/YSZ interface region. The structural change at the electrode/YSZ interface region was also observed by Kuznecov et al. [161] on LSM cathode and by Kusnezoff et al. [232] on LSM/YSZ composite cathode. Weber et al. [233] operated LSM cathodes at 950 °C for ~2000 h and observed the considerable microstructural changes such as grain growth, densification, and migration of Mn out of the cathode and into the electrolyte. However, the overall performance degradation of the cell was 70 mV over 2543 h and the contribution from the LSM cathode side should be small.

Sholklapper et al. [234] studied the structure and performance stability of a nanoparticle-infiltrated LSM in porous scandia-stabilized zirconia (SSZ) electrode at 650 °C. The infiltrated LSM particles are ~100 nm in diameter and some orientation alignment of the LSM nanoparticles within SSZ is observed after the cathodic polarization at 150 mA cm^{-2} for 500 h. There is no voltage degradation under the conditions studied.

The performance and stability of LSM cathode can also be enhanced by increasing the LSM cathode/YSZ electrolyte interface via interlocking electrolyte and cathode. Herbstritt et al. [235] modified the YSZ electrolyte surface by screen printing a porous monolayer of individual YSZ particles (particle size = ~17 μm) onto the electrolyte substrate. The structured electrolyte surface is covered with a thin LSM MOD (metallo-organic-deposition, ~80 nm thick) layer, followed by a screen-printed LSM cathode

layer. Single cells with the modified LSM cathodes showed improved long-term stability due to the better adhesion of the cathode layer; the degradation of the cells with modified LSM cathode is 14 mV/1000 h during the long-term operation at 300 mA cm^{-2}, much lower than 35 mV/1000 h of a standard cell under the same test conditions.

The stability or shelf-life of the electrode powder, ink, and coating is important for the stability and reproducibility of the cell performance. Bergsmark et al. [236] studied the stability of LSM powder with a small lanthanum excess (A-site over-stoichiometry) and found that the pellets prepared from the powder disintegrated after exposure to air, due to the formation of $La(OH)_3$. Stability of LSM powder decreases with increasing (La + Sr)/Mn ratio. Jiang et al. [106] investigated in detail the shelf-life of LSM materials under storage conditions of low and high humidity at ambient temperature for ~350 days. It has been found that the adhesion and stability of the electrode performance of LSM materials are critically dependent on the A-site stoichiometry (i.e., (La + Sr)/Mn ratio) of the LSM materials and much less on the storage conditions (humidity level and storage time) over the period investigated. The results demonstrate that LSM materials with A-site sub-stoichiometry ((La + Sr)/Mn = ~0.9) are effective in achieving good adherence, high chemical stability, and high stability of electrode performance.

Concluding remarks

Lanthanum strontium manganite (LSM)-based perovskite is the most important electrode material in SOFCs. The polarization performance and electrochemical activity of LSM-based cathodes is a complex function of composition, microstructure, electrode/electrolyte interface, and the activation effect. In addition, the polarization performance of LSM cathodes is also affected by external testing parameters such as the cell size, the contacts between the current collector and LSM electrode, the mechanical loading, etc. There has been a quantum leap in the fundamental understanding on the processing–microstructure–property relations for LSM and LSM/YSZ or LSM/GDC composite electrode materials and this has played an important and critical role in the design and tailoring of the LSM-based cathode for high-temperature SOFC development in the last 20–30 years.

The sustained interesting and enthusiasm about this material arises from the fact that LSM has distinctive advantages as cathodes of high-temperature SOFCs: its high electrical conductivity, high electrochemical activity for the O_2 reduction reaction, high thermal stability and compatibility with the common SOFC electrolytes of YSZ, GDC, and LSGM at SOFC operating conditions. Most important among the cathode materials, LSM has an excellent track record of microstructural stability and long-term performance stability. The fundamental reason for the long-term stability of LSM-based electrodes is most likely the significantly reduced cation vacancies under SOFC operating conditions, leading to the significant increased sintering resistance of the LSM-based electrode materials [228]. The electrocatalytic activity of LSM-based materials can also be substantially enhanced by the nano-structured approach, e.g., by infiltration and impregnation of catalytic active and MIEC nanoparticles. The performance of nano-structured LSM-based electrodes is comparable to that of typical MIEC electrodes such as LSCF in the intermediate temperatures of 700–900 °C (see Fig. 24). In the case of SOFCs using Fe–Cr alloy metallic interconnect, Cr poisoning and deposition are serious concerns for the LSM-based perovskite cathodes. However, the use of LSM/GDC and GDC-impregnated LSM composite cathodes can significantly reduce the Cr deposition and Cr poisoning effect [141].

As shown in this review, one of the critical challenges for the operation of SOFC at intermediate and low temperatures is to reduce the interface polarization resistance. The conventional composite electrode approach needs high sintering temperatures to form an intimate electrode/electrolyte interface and the high processing temperature, unfortunately, limits the options in the optimization of the microstructure of the cathode. Therefore, the development of alternative synthesis method for the LSM-based composite electrodes is essential to create not only a macroscopically homogeneous composite material, but also a nano-structured material. Nano-particles and well-designed structure with dimensions of 20 nm or smaller would serve to substantially increase the TPB and also to increase the thermal stability, as the domain growth of either component may be effectively limited by the growth of the second component. Nano-structured LSM-based electrode materials amalgamated with high surface area and sufficient porosity offer superior electrochemical properties and have great potentials as cathodes of intermediate- and low-temperature SOFCs.

Another challenge in the development of LSM-based electrode materials for intermediate- and low-temperature SOFC is the high activation energy for the O_2 reduction reaction. The high activation energy leads to the substantial increase in the electrode polarization resistance as the operating temperature reduces. The critical question is whether it is possible to reduce the activation energy for the O_2 reduction reaction on LSM-based cathodes? We [237] recently studied the impregnated Pd/YSZ electrode and found that the activation energy for the O_2 reduction reaction on nano-structured Pd/YSZ cathode is 105 kJ mol^{-1} that is significantly smaller than 130–210 kJ mol^{-1} for the reaction on conventional cathodes such as LSM, LSM/YSZ,

LSM/GDC, LSCF, and (Gd,Sr)CoO_3 (GSC) [90, 157, 167, 189, 191, 238]. The low activation energy may indicate the change in the reaction mechanism and kinetics for the O_2 reduction on nano-structured Pd/YSZ composite cathode. Thus, it is possible to decrease the activation energy for the reaction on LSM-based electrodes by introducing electrocatalytically active and nano-sized phase for the O_2 reduction reaction.

Beyond testing in small button cells, the viability of new LSM-based cathode materials must ultimately be proven in large-scale stack cells under practical current and temperature gradients. Issues involved in the development of cathode materials for large-scale stacks are significantly more complex than that in the small button cells which are briefly reviewed in this article. This does provide serious challenges as well as opportunities for materials scientists and engineers in the development of commercially viable ITSOFCs technologies based on LSM cathodes.

References

1. Yokokawa H, Sakai N, Horita T, Yamaji K, Brito ME (2005) Mater Res Soc Bull 30:591
2. Jiang SP, Chan SH (2004) J Mater Sci 39:4405. doi:10.1023/B:JMSC.0000034135.52164.6b
3. Gorte RJ, Vohs JM, McIntosh S (2004) Solid State Ionics 175:1. doi:10.1016/j.ssi.2004.09.036
4. Adler SB (2004) Chem Rev 104:4791. doi:10.1021/cr020724o
5. Fergus JW (2005) Mater Sci Eng A Struct Mater Prop Microstruct Process 397:271
6. De Jonghe LC, Jacobson CP, Visco SJ (2003) Annu Rev Mater Res 33:169. doi:10.1146/annurev.matsci.33.041202.103842
7. Ivers-Tiffee E, Weber A, Herbstritt D (2001) J Eur Ceram Soc 21:1805. doi:10.1016/S0955-2219(01)00120-0
8. Tofield BC, Scott WR (1974) J Solid State Chem 10:183. doi:10.1016/0022-4596(74)90025-5
9. Hammouche A, Siebert E, Hammou A (1989) Mater Res Bull 24:367. doi:10.1016/0025-5408(89)90223-7
10. Shannon RD (1976) Acta Crystallogr A 32:751. doi:10.1107/S0567739476001551
11. Li Z, Behruzi M, Fuerst L, Stover D (1993) In: Singhal SC, Iwahara H (eds) SOFC-III. The Electrochemical Society, Inc., Pennington. p 171
12. Zhang ZT, Lin OY, Tang ZL (1995) In: Dokiya M, Tagawa H, Singhal SC (eds) SOFC-IV. The Electrochemical Society, Pennington, p 502
13. Zheng F, Pederson LR (1999) J Electrochem Soc 146:2810. doi:10.1149/1.1392012
14. Jiang SP, Love JG, Zhang JP, Hoang M, Ramprakash Y, Hughes AE et al (1999) Solid State Ionics 121:1. doi:10.1016/S0167-2738(98)00295-1
15. Mizusaki J, Tagawa H, Naraya K, Sasamoto T (1991) Solid State Ionics 49:111. doi:10.1016/0167-2738(91)90076-N
16. Mizusaki J (1992) Solid State Ionics 52:79. doi:10.1016/0167-2738(92)90093-5
17. Mizusaki J, Mori N, Takai H, Yonemura Y, Minamiue H, Tagawa H et al (2000) Solid State Ionics 129:163. doi:10.1016/S0167-2738(99)00323-9
18. Mizusaki J, Yonemura Y, Kamata H, Ohyama K, Mori N, Takai H et al (2000) Solid State Ionics 132:167. doi:10.1016/S0167-2738(00)00662-7
19. Miyoshi S, Hong JO, Yashiro K, Kaimai A, Nigara Y, Kawamura K et al (2002) Solid State Ionics 154:257. doi:10.1016/S0167-2738(02)00441-1
20. van Roosmalen JAM, Cordfunke EHP, Helmholdt RB, Zandbergen HW (1994) J Solid State Chem 110:100. doi:10.1006/jssc.1994.1141
21. Mitchell JF, Argyriou DN, Potter CD, Hinks DG, Jorgensen JD, Bader SD (1996) Phys Rev B 54:6172. doi:10.1103/PhysRevB.54.6172
22. Alonso JA, Martinez-Lope MJ, Casais MT, MacManus-Driscoll JL, de Silva P, Cohen LF, Fernandez Diaz MT (1997) J Mater Chem 7:2139. doi:10.1039/a704088a
23. Nowotny J, Rekas M (1998) J Am Ceram Soc 81:67
24. Huang Q, Santoro A, Lynn JW, Erwin RW, Borchers JA, Peng JL et al (1997) Phys Rev B 55:14987. doi:10.1103/PhysRevB.55.14987
25. De Souza RA, Islam MS, Ivers-Tiffee E (1999) J Mater Chem 9:1621. doi:10.1039/a901512d
26. van Roosmalen JAM, Cordfunke EHP (1994) J Solid State Chem 110:109. doi:10.1006/jssc.1994.1143
27. van Roosmalen JAM, Cordfunke EHP (1994) J Solid State Chem 110:113. doi:10.1006/jssc.1994.1144
28. van Roosmalen JAM, Cordfunke EHP (1994) J Solid State Chem 110:106. doi:10.1006/jssc.1994.1142
29. Nakamura K, Xu MX, Klaser M, Linker G (2001) J Solid State Chem 156:143. doi:10.1006/jssc.2000.8974
30. Nakamura K, Ogawa K (2002) J Solid State Chem 163:65. doi:10.1006/jssc.2001.9370
31. Alonso JA, MartinezLope MJ, Casais MT (1996) Eur J Solid State Inorg Chem 33:331
32. Miyoshi S, Hong JO, Yashiro K, Kaimai A, Nigara Y, Kawamura K et al (2003) Solid State Ionics 161:209. doi:10.1016/S0167-2738(03)00281-9
33. Kuo JH, Anderson HU, Sparlin DM (1989) J Solid State Chem 83:52. doi:10.1016/0022-4596(89)90053-4
34. Kuo JH, Anderson HU, Sparlin DM (1990) J Solid State Chem 87:55. doi:10.1016/0022-4596(90)90064-5
35. Kamata H, Yonemura Y, Mizusaki J, Tagawa H, Naraya K, Sasamoto T (1995) J Phys Chem Solids 56:943. doi:10.1016/0022-3697(95)00019-4
36. Yasumoto K, Shiono M, Tagawa H, Dokiya M, Hirano K, Mizusaki J (2002) J Electrochem Soc 149:A531. doi:10.1149/1.1463400
37. Yasumoto K, Mori N, Mizusaki J, Tagawa H, Dokiya M (2001) J Electrochem Soc 148:A105. doi:10.1149/1.1344524
38. Lee HY, Cho WS, Oh SM, Wiemhofer HD, Gopel W (1995) J Electrochem Soc 142:2659. doi:10.1149/1.2050070
39. Hammouche A, Siebert E, Hammou A, Kleitz M, Caneiro A (1991) J Electrochem Soc 138:1212. doi:10.1149/1.2085761
40. Chen XJ, Chan SH, Khor KA (2004) Electrochem Solid-State Lett 7:A144. doi:10.1149/1.1701584
41. Wang W, Jiang SP (2006) Solid State Ionics 177:1361. doi:10.1016/j.ssi.2006.05.022
42. Jiang SP, Love JG (2001) Solid State Ionics 138:183. doi:10.1016/S0167-2738(00)00806-7
43. Caillol N, Pijolat M, Siebert E (2007) Appl Surf Sci 253:4641. doi:10.1016/j.apsusc.2006.10.019
44. Wu QH, Liu ML, Jaegermann W (2005) Mater Lett 59:1980. doi:10.1016/j.matlet.2005.01.038
45. Egdell RG, Harrison MR, Hill MD, Porte L, Wall G (1984) J Phys C Solid State Phys 17:2889. doi:10.1088/0022-3719/17/16/008

46. Kemp JP, Beal DJ, Cox PA (1990) J Solid State Chem 86:50. doi:10.1016/0022-4596(90)90112-B
47. Howlett JF, Flavell WR, Thomas AG, Hollingworth J, Warren S, Hashim Z et al (1996) Faraday Discuss 105:337. doi:10.1039/fd9960500337
48. Jiang SP (2006) J Solid State Electrochem 11:93. doi:10.1007/s10008-005-0076-9
49. Hammouche A, Schouler EJL, Henault M (1988) Solid State Ionics 28:1205. doi:10.1016/0167-2738(88)90358-X
50. Yokokawa H, Sakai N, Kawada T, Dokiya M (1990) Solid State Ionics 40–41:398. doi:10.1016/0167-2738(90)90366-Y
51. Otoshi S, Sasaki H, Ohnishi H, Hase M, Ishimaru K, Ippommatsu M et al (1991) J Electrochem Soc 138:1519. doi:10.1149/1.2085819
52. Mattiot FP, Giunta G, Selvaggi A (1994) In: Uossel U (ed) First European SOFC forum. European Fuel Cell Group, Ltd, Lucerne, p 735
53. Jiang SP, Love JG, Apateanu L (2003) Solid State Ionics 160:15. doi:10.1016/S0167-2738(03)00127-9
54. Aruna ST, Muthuraman M, Patil KC (1997) J Mater Chem 7:2499. doi:10.1039/a703901h
55. Mori M, Hiei Y, Sammes NM, Tompsett GA (1999) In: Singhal S, Dokiya M (eds) SOFC-VI. The Electrochemical Society, Inc., Pennington, p 347
56. Anderson HU (1992) Solid State Ionics 52:33. doi:10.1016/0167-2738(92)90089-8
57. Minh NQ (1993) J Am Ceram Soc 76:563. doi:10.1111/j.1151-2916.1993.tb03645.x
58. Berenov A, Wood H, Atkinson A (2007) ECS Trans 7:1173. doi:10.1149/1.2729216
59. Kuharuangrong S, Dechakupt T, Aungkavattana P (2004) Mater Lett 58:1964. doi:10.1016/j.matlet.2003.12.011
60. Sakaki Y, Takeda Y, Kato A, Imanishi N, Yamamoto O, Hattori M et al (1999) Solid State Ionics 118:187. doi:10.1016/S0167-2738(98)00440-8
61. Kostogloudis GC, Ftikos C (1999) J Eur Ceram Soc 19:497. doi:10.1016/S0955-2219(98)00221-0
62. Rim HR, Jeung SK, Jung E, Lee JS (1998) Mater Chem Phys 52:54. doi:10.1016/S0254-0584(98)80006-0
63. Kostogloudis GC, Vasilakos N, Ftikos C (1997) J Eur Ceram Soc 17:1513. doi:10.1016/S0955-2219(97)00038-1
64. Yoon HS, Choi SW, Lee D, Kim BH (2001) J Power Sources 93:1. doi:10.1016/S0378-7753(00)00504-8
65. Phillipps MB, Sammes NM, Yamamoto O (1999) Solid State Ionics 123:131. doi:10.1016/S0167-2738(99)00082-X
66. Hashimoto S, Iwahara H (2000) J Electroceram 4:225. doi:10.1023/A:1009936515152
67. Wandekar RV, Wani BN, Bharadwaj SR (2005) Mater Lett 59:2799. doi:10.1016/j.matlet.2005.03.062
68. Kuharuangrong S (2004) Ceram Int 30:273. doi:10.1016/S0272-8842(03)00099-3
69. Moure C, Gutierrez D, Tartaj J, Duran P (2003) J Eur Ceram Soc 23:729. doi:10.1016/S0955-2219(02)00165-6
70. Nasrallah MM, Carter JD, Anderson HU, Koc R (1991) In: Grosz F, Zegers P, Singhal SC, Yamamoto O (eds) SOFC-II. Commission of the European Communities, Luxemburg, p 637
71. Jiang SP, Liu L, Ong KP, Wu P, Li J, Pu J (2008) J Power Sources 176:82
72. Kim JD, Kim GD, Moon JW, Park YI, Lee WH, Kobayashi K et al (2001) Solid State Ionics 143:379. doi:10.1016/S0167-2738(01)00877-3
73. Ji Y, Kilner JA, Carolan MF (2005) Solid State Ionics 176:937. doi:10.1016/j.ssi.2004.11.019
74. Yang CCT, Wei WCJ, Roosen A (2003) Mater Chem Phys 81:134. doi:10.1016/S0254-0584(03)00158-5
75. Carter S, Selcuk A, Chater RJ, Kajda J, Kilner JA, Steele BCH (1992) Solid State Ionics 53–56:597. doi:10.1016/0167-2738(92)90435-R
76. De Souza RA, Kilner JA, Walker JF (2000) Mater Lett 43:43. doi:10.1016/S0167-577X(99)00228-1
77. Berenov AV, MacManus-Driscoll JL, Kilner JA (1999) Solid State Ionics 122:41. doi:10.1016/S0167-2738(99)00077-6
78. Horita T, Tsunoda T, Yamaji K, Sakai N, Kato T, Yokokawa H (2002) Solid State Ionics 152:439. doi:10.1016/S0167-2738(02)00367-3
79. Horita T, Yamaji K, Ishikawa M, Sakai N, Yokokawa H, Kawada T et al (1998) J Electrochem Soc 145:3196. doi:10.1149/1.1838786
80. Yasuda I, Ogasawara K, Hishinuma M, Kawada T, Dokiya M (1996) Solid State Ionics 86–88:1197. doi:10.1016/0167-2738(96)00287-1
81. Yamahara K, Sholklapper TZ, Jacobson CP, Visco SJ, De Jonghe LC (2005) Solid State Ionics 176:1359. doi:10.1016/j.ssi.2005.03.010
82. Belzner A, Gur TM, Huggins RA (1992) Solid State Ionics 57:327. doi:10.1016/0167-2738(92)90166-M
83. Lade K, Jacobsen T (1994) Solid State Ionics 72:218. doi:10.1016/0167-2738(94)90150-3
84. Badwal SPS, Jiang SP, Love J, Nowotny J, Rekas M, Vance ER (2001) Ceram Int 27:431. doi:10.1016/S0272-8842(00)00098-5
85. Badwal SPS, Jiang SP, Love J, Nowotny J, Rekas M, Vance ER (2001) Ceram Int 27:419. doi:10.1016/S0272-8842(00)00097-3
86. Kopp A, Nafe H, Weppner W (1992) Solid State Ionics 53–56:853. doi:10.1016/0167-2738(92)90265-Q
87. Endo A, Ihara M, Komiyama H, Yamada K (1996) Solid State Ionics 86–88:1191. doi:10.1016/0167-2738(96)00286-X
88. Ullmann H, Trofimenko N, Tietz F, Stover D, Ahmad-Khanlou A (2000) Solid State Ionics 138:79. doi:10.1016/S0167-2738(00)00770-0
89. Godoi GS, de Souza DPF (2007) Mater Sci Eng B Solid State Mater Adv Technol 140:90
90. Jiang SP (2002) Solid State Ionics 146:1. doi:10.1016/S0167-2738(01)00997-3
91. Meixner DL, Cutler RA (2002) Solid State Ionics 146:273. doi:10.1016/S0167-2738(01)01027-X
92. Atkinson A, Selcuk A (2000) Solid State Ionics 134:59. doi:10.1016/S0167-2738(00)00714-1
93. D'Souza CM, Sammes NM (2000) J Am Ceram Soc 83:47. doi:10.1111/j.1151-2916.2000.tb01146.x
94. Meixner DL, Cutler RA (2002) Solid State Ionics 146:285. doi:10.1016/S0167-2738(01)01028-1
95. Yokokawa H, Sakai N, Kawada T, Dokiya M (1991) J Electrochem Soc 138:2719. doi:10.1149/1.2086043
96. Yokokawa H, Horita T, Sakai N, Dokiya M, Kawada T (1996) Solid State Ionics 86–88:1161. doi:10.1016/0167-2738(96)00281-0
97. Yokokawa H, Sakai N, Kawada T, Dokiya M (1993) In: Badwal SPS, Bannister MJ, Hannink RHJ (eds) Science and technology of zirconia V. Technomic Publishing Company, Inc., Melbourne, p 752
98. Yokokawa H (2003) Annu Rev Mater Res 33:581. doi:10.1146/annurev.matsci.33.022802.093856
99. Tsai T, Barnett SA (1997) Solid State Ionics 93:207. doi:10.1016/S0167-2738(96)00524-3
100. Mitterdorfer A, Gauckler LJ (1998) Solid State Ionics 111:185. doi:10.1016/S0167-2738(98)00195-7
101. Stochniol G, Syskakis E, Naoumidis A (1995) J Am Ceram Soc 78:929. doi:10.1111/j.1151-2916.1995.tb08416.x
102. Lau SK, Singhal SC (1985) In: Corrosion 85. The National Association of Corrosion Engineers, Houston, p 1

103. Brugnoni C, Ducati U, Scagliotti M (1995) Solid State Ionics 76:177. doi:10.1016/0167-2738(94)00299-8
104. Taimatsu H, Wada K, Kaneko H, Yamamura H (1992) J Am Ceram Soc 75:401. doi:10.1111/j.1151-2916.1992.tb08193.x
105. Tricker DM, Stobbs WM (1993) In: Poulsen FW, Bentzen JJ, Jacobsen T, Skou E, Ostergard MJL (eds) 14th Riso international symposium on materials science: high temperature electrochemical behaviour of fast ion and mixed conductors. Riso National Laboratory, Roskilde, p 453
106. Jiang SP, Zhang JP, Ramprakash Y, Milosevic D, Wilshier K (2000) J Mater Sci 35:2735. doi:10.1023/A:1004766212164
107. Kenjo T, Nishiya M (1992) Solid State Ionics 57:295. doi:10.1016/0167-2738(92)90161-H
108. Yamamoto O, Takeda Y, Kanno R, Kojima T (1989) In: Singhal SC (ed) SOFC-I. The Electrochemical Society, Inc., Pennington, p 242
109. Mori M, Abe T, Itoh H, Yamamoto O, Shen GQ, Takeda Y et al (1999) Solid State Ionics 123:113. doi:10.1016/S0167-2738(99)00115-0
110. Jiang SP, Zhang JP, Foger K (2003) J Eur Ceram Soc 23:1865. doi:10.1016/S0955-2219(02)00447-8
111. Kawada T, Sakai N, Yokokawa H, Dokiya M, Anzai I (1992) Solid State Ionics 50:189. doi:10.1016/0167-2738(92)90218-E
112. Waller D, Sirman JD, Kilner JA (1997) In: Stimming U, Singhal SC, Tagawa H, Lehnert W (eds) SOFC-V. The Electrochemical Society, Inc., Pennington
113. Clausen C, Bagger C, Bildesorensen JB, Horsewell A (1994) Solid State Ionics 70:59. doi:10.1016/0167-2738(94)90287-9
114. Yamamoto O, Shen GQ, Takeda Y, Imanishi N, Sakaki Y (1991) In: SOFC-II. The Electrochemical Society, Inc., Pennington, p 158
115. van Roosmalen JAM, Cordfunke EHP (1992) Solid State Ionics 52:303. doi:10.1016/0167-2738(92)90177-Q
116. Zhang JP, Jiang SP, Love JG, Foger K, Badwal SPS (1998) J Mater Chem 8:2787. doi:10.1039/a805835k
117. Khandkar A, Elangovan S, Liu M (1992) Solid State Ionics 52:57. doi:10.1016/0167-2738(92)90091-3
118. Mitsuyasu H, Eguchi K, Arai H (1997) Solid State Ionics 100:11. doi:10.1016/S0167-2738(97)00343-3
119. Labrincha JA, Frade JR, Marques FMB (1993) J Mater Sci 28:3809. doi:10.1007/BF00353183
120. Wagner C (1933) Z Phys Chem B 21:25
121. Poulsen FW, Vanderpuil N (1992) Solid State Ionics 53–56:777
122. Ciacchi FT, Crane KM, Badwal SPS (1994) Solid State Ionics 73:49. doi:10.1016/0167-2738(94)90263-1
123. Takeda Y, Tu HY, Sakaki H, Watanabe S, Imanishi N, Yamamoto O et al (1997) J Electrochem Soc 144:2810. doi:10.1149/1.1837899
124. Huang KQ, Feng M, Goodenough JB, Schmerling M (1996) J Electrochem Soc 143:3630. doi:10.1149/1.1837262
125. Naoumidis A, Ahmad-Khanlou A, Samardzija Z, Kolar D (1999) Fresenius J Anal Chem 365:277. doi:10.1007/s002160051488
126. Pelosato R, Sora IN, Dotelli G, Ruffo R, Mari CM (2005) J Eur Ceram Soc 25:2587. doi:10.1016/j.jeurceramsoc.2005.03.107
127. Ullmann H, Trofimenko N, Naoumidis A, Stover D (1999) J Eur Ceram Soc 19:791. doi:10.1016/S0955-2219(98)00315-X
128. Badwal SPS, Deller R, Foger K, Ramprakash Y, Zhang JP (1997) Solid State Ionics 99:297. doi:10.1016/S0167-2738(97)00247-6
129. Taniguchi S, Kadowaki M, Kawamura H, Yasuo T, Akiyama Y, Miyake Y et al (1995) J Power Sources 55:73. doi:10.1016/0378-7753(94)02172-Y
130. Paulson SC, Birss VI (2004) J Electrochem Soc 151:A1961. doi:10.1149/1.1806392
131. Matsuzaki Y, Yasuda I (2000) Solid State Ionics 132:271. doi:10.1016/S0167-2738(00)00654-8
132. Matsuzaki Y, Yasuda I (2001) J Electrochem Soc 148:A126. doi:10.1149/1.1339869
133. Hilpert K, Das D, Miller M, Peck DH, Weiss R (1996) J Electrochem Soc 143:3642. doi:10.1149/1.1837264
134. Konysheva E, Penkalla H, Wessel E, Mertens J, Seeling U, Singheiser L et al (2006) J Electrochem Soc 153:A765. doi:10.1149/1.2172563
135. Jiang SP, Zhang JP, Foger K (2001) J Electrochem Soc 148:C447. doi:10.1149/1.1374446
136. Jiang SP, Zhang JP, Apateanu L, Foger K (1999) Electrochem Commun 1:394. doi:10.1016/S1388-2481(99)00080-6
137. Jiang SP, Zhang JP, Apateanu L, Foger K (2000) J Electrochem Soc 147:4013. doi:10.1149/1.1394012
138. Jiang SP, Zhang JP, Zheng XG (2002) J Eur Ceram Soc 22:361. doi:10.1016/S0955-2219(01)00280-1
139. Jiang SP, Zhang S, Zhen YD (2005) J Mater Res 20:747. doi:10.1557/JMR.2005.0101
140. Jiang SP, Wang W (2005) Electrochem Solid-State Lett 8:A115. doi:10.1149/1.1847689
141. Jiang SP, Zhen YD, Zhang S (2006) J Electrochem Soc 153:A1511. doi:10.1149/1.2207060
142. Quadakkers WJ, Greiner H, Hansel M, Pattanaik A, Khanna AS, Mallener W (1996) Solid State Ionics 91:55. doi:10.1016/S0167-2738(96)00425-0
143. Zhen YD, Jiang SP, Zhang S, Tan V (2006) J Eur Ceram Soc 26:3253. doi:10.1016/j.jeurceramsoc.2005.10.002
144. Kim JH, Song RH, Hyun SH (2004) Solid State Ionics 174:185. doi:10.1016/j.ssi.2004.07.032
145. Fujita K, Ogasawara K, Matsuzaki Y, Sakurai T (2004) J Power Sources 131:261. doi:10.1016/j.jpowsour.2003.12.051
146. Huang KQ, Hou PY, Goodenough JB (2000) Solid State Ionics 129:237. doi:10.1016/S0167-2738(99)00329-X
147. Chen X, Hou PY, Jacobson CP, Visco SJ, De Jonghe LC (2005) Solid State Ionics 176:425. doi:10.1016/j.ssi.2004.10.004
148. Li JQ, Xiao P (2001) J Eur Ceram Soc 21:659. doi:10.1016/S0955-2219(00)00242-9
149. Lahl N, Singheiser L, Hilpert K (1999) In: Singhal SC, Dokiya M (eds) SOFC-VI. The Electrochemical Society, Inc., Pennington, p 1057
150. Gunther C, Hofer G, Kleinlein W (1997) In: Stimming U, Singhal SC, Tagawa H, Lehnert W (eds) SOFC-V. The Electrochemical Society, Inc., Pennington, p 746
151. Jiang SP, Christiansen L, Hughan B, Foger K (2001) J Mater Sci Lett 20:695. doi:10.1023/A:1010950722533
152. van Heuveln FH, Bouwmeester HJM (1997) J Electrochem Soc 144:134. doi:10.1149/1.1837375
153. Chen XJ, Khor KA, Chan SH (2004) Solid State Ionics 167:379. doi:10.1016/j.ssi.2003.08.049
154. Kikuchi R, Murakami K, Futamura M, Matsui T, Eguchi K (2007) ECS Trans 7:1251. doi:10.1149/1.2729226
155. McEvoy AJ (2000) Solid State Ionics 135:331. doi:10.1016/S0167-2738(00)00460-4
156. Haanappel VAC, Mai A, Mertens J (2006) Solid State Ionics 177:2033. doi:10.1016/j.ssi.2005.12.038
157. Leng YJ, Chan SH, Khor KA, Jiang SP (2004) J Appl Electrochem 34:409. doi:10.1023/B:JACH.0000016627.29374.24
158. Lee YK, Kim JY, Lee YK, Kim I, Moon HS, Park JW et al (2003) J Power Sources 115:219. doi:10.1016/S0378-7753(02)00727-9
159. McIntosh S, Adler SB, Vohs JM, Gorte RJ (2004) Electrochem Solid-State Lett 7:A111. doi:10.1149/1.1667792
160. Tsukuda H, Yamashita H (1994) In: Bossel U (ed) First European SOFC forum. European Fuel Cells Group, Lucerne, p 715

161. Kuznecov M, Otschik P, Obenaus P, Eichler K, Schaffrath W (2003) Solid State Ionics 157:371. doi:10.1016/S0167-2738(02)00235-7
162. Wang W, Jiang SP (2004) J Solid State Electrochem 8:914. doi:10.1007/s10008-004-0515-z
163. Jiang SP, Love JG (2003) Solid State Ionics 158:45. doi:10.1016/S0167-2738(02)00760-9
164. Siebert E, Hammouche A, Kleitz M (1995) Electrochim Acta 40:1741. doi:10.1016/0013-4686(94)00361-4
165. Jiang Y, Wang SZ, Zhang YH, Yan JW, Li WZ (1998) J Electrochem Soc 145:373. doi:10.1149/1.1838271
166. Gharbage B, Pagnier T, Hammou A (1994) J Electrochem Soc 141:2118. doi:10.1149/1.2055071
167. Jiang SP, Zhang JP, Foger K (2000) J Electrochem Soc 147:3195. doi:10.1149/1.1393883
168. Jiang SP, Love JG, Ramprakash Y (2002) J Power Sources 110:201. doi:10.1016/S0378-7753(02)00259-8
169. Mizusaki J, Tagawa H, Tsuneyoshi K, Sawata A (1991) J Electrochem Soc 138:1867. doi:10.1149/1.2085891
170. van Heuveln FH, Bouwmeester HJM, van Berkel FPF (1997) J Electrochem Soc 144:126. doi:10.1149/1.1837374
171. Fukunaga H, Ihara M, Sakaki K, Yamada K (1996) Solid State Ionics 86–88:1179. doi:10.1016/0167-2738(96)00284-6
172. Sasaki K, Gauckler LJ (1996) Denki Kagaku 64:654
173. Sasaki K, Wurth JP, Gschwend R, Godickemeier M, Gauckler LJ (1996) J Electrochem Soc 143:530. doi:10.1149/1.1836476
174. Lee HK (2002) Mater Chem Phys 77:639. doi:10.1016/S0254-0584(02)00091-3
175. Yamamoto O, Takeda Y, Kanno R, Noda M (1987) Solid State Ionics 22:241. doi:10.1016/0167-2738(87)90039-7
176. Takeda Y, Kanno R, Noda M, Tomida Y, Yamamoto O (1987) J Electrochem Soc 134:2656. doi:10.1149/1.2100267
177. Ishihara T, Kudo T, Matsuda H, Takita Y (1994) J Am Ceram Soc 77:1682. doi:10.1111/j.1151-2916.1994.tb09779.x
178. Ishihara T, Kudo T, Matsuda H, Takita Y (1995) J Electrochem Soc 142:1519. doi:10.1149/1.2048606
179. Huang XQ, Liu J, Lu Z, Liu W, Pei L, He TM et al (2000) Solid State Ionics 130:195. doi:10.1016/S0167-2738(00)00643-3
180. Hayashi K, Yamamoto O, Nishigaki Y, Minoura H (1997) Solid State Ionics 98:49. doi:10.1016/S0167-2738(97)00098-2
181. Xia CR, Zhang YL, Liu ML (2003) Electrochem Solid-State Lett 6:A290. doi:10.1149/1.1621830
182. Choi JH, Jang JH, Oh SM (2001) Electrochim Acta 46:867. doi:10.1016/S0013-4686(00)00666-6
183. Jorgensen MJ, Primdahl S, Bagger C, Mogensen M (2001) Solid State Ionics 139:1. doi:10.1016/S0167-2738(00)00818-3
184. Barbucci A, Viviani M, Carpanese P, Vladikova D, Stoynov Z (2006) Electrochim Acta 51:1641. doi:10.1016/j.electacta.2005.02.106
185. Co AC, Xia SJ, Birss VI (2005) J Electrochem Soc 152:A570. doi:10.1149/1.1859612
186. Kamata H, Hosaka A, Mizusaki J, Tagawa H (1998) Solid State Ionics 106:237. doi:10.1016/S0167-2738(97)00495-5
187. Zhen YD, Jiang SP (2006) J Electrochem Soc 153:A2245. doi:10.1149/1.2357712
188. Suzuki T, Awano M, Jasinski P, Petrovsky V, Anderson HU (2006) Solid State Ionics 177:2071. doi:10.1016/j.ssi.2005.12.016
189. Murray EP, Tsai T, Barnett SA (1998) Solid State Ionics 110:235. doi:10.1016/S0167-2738(98)00142-8
190. Song HS, Kim WH, Hyun SH, Moon J, Kim J, Lee HW (2007) J Power Sources 167:258. doi:10.1016/j.jpowsour.2007.01.095
191. Murray EP, Barnett SA (2001) Solid State Ionics 143:265. doi:10.1016/S0167-2738(01)00871-2
192. Xia CR, Rauch W, Wellborn W, Liu ML (2002) Electrochem Solid-State Lett 5:A217. doi:10.1149/1.1503203
193. Zhao H, Huo LH, Gao S (2004) J Power Sources 125:149. doi:10.1016/j.jpowsour.2003.07.009
194. Yi JY, Choi GM (2004) J Eur Ceram Soc 24:1359. doi:10.1016/S0955-2219(03)00569-7
195. Armstrong TJ, Virkar AV (2002) J Electrochem Soc 149:A1565. doi:10.1149/1.1517282
196. Pena-Martinez J, Marrero-Lopez D, Ruiz-Morales JC, Buergler BE, Nunez P, Gauckler LJ (2006) J Power Sources 159:914. doi:10.1016/j.jpowsour.2005.11.036
197. Tanner CW, Fung KZ, Virkar AV (1997) J Electrochem Soc 144:21. doi:10.1149/1.1837360
198. Liu Y, Zha SW, Liu ML (2004) Adv Mater 16:256. doi:10.1002/adma.200305767
199. Jiang SP (2006) Mater Sci Eng A Struct Mater Prop Microstruct Process 418:199
200. Jiang SP, Wang W (2005) Solid State Ionics 176:1351. doi:10.1016/j.ssi.2005.03.011
201. Jiang SP, Wang W (2005) J Electrochem Soc 152:A1398. doi:10.1149/1.1928167
202. Yamahara K, Jacobson CP, Visco SJ, Zhang XF, de Jonghe LC (2005) Solid State Ionics 176:275. doi:10.1016/j.ssi.2004.08.017
203. Juhl M, Primdahl S, Manon C, Mogensen M (1996) J Power Sources 61:173. doi:10.1016/S0378-7753(96)02361-0
204. Holtappels P, Bagger C (2002) J Eur Ceram Soc 22:41. doi:10.1016/S0955-2219(01)00238-2
205. Liu Y, Compson C, Liu ML (2004) J Power Sources 138:194. doi:10.1016/j.jpowsour.2004.06.035
206. Hibino T, Hashimoto A, Inoue T, Tokuno J, Yoshida S, Sano M (2000) Science 288:2031. doi:10.1126/science.288.5473.2031
207. Morel B, Roberge R, Savoie S, Napporn TW, Meunier M (2007) Appl Catal Gen 323:181. doi:10.1016/j.apcata.2007.02.020
208. Demin AK, Gulbis FY (2000) Solid State Ionics 135:451. doi:10.1016/S0167-2738(00)00395-7
209. van Heuveln FH (1994) J Electrochem Soc 141:3423. doi:10.1149/1.2059348
210. Tannenberger H, Siegert H (1969) Adv Chem Ser 90:281
211. Itagaki Y, Matsubara F, Asamoto M, Yamaura H, Yahiro H, Sadaoka Y (2007) ECS Trans 7:1319. doi:10.1149/1.2729235
212. Jiang SP (2003) J Power Sources 124:390. doi:10.1016/S0378-7753(03)00814-0
213. Jiang SP (2001) J Electrochem Soc 148:A887. doi:10.1149/1.1383776
214. Uchida H, Yoshida M, Watanabe M (1999) J Electrochem Soc 146:1. doi:10.1149/1.1391555
215. Tsai T, Barnett SA (1997) Solid State Ionics 98:191. doi:10.1016/S0167-2738(97)00113-6
216. Kawagoe Y, Namie S, Nomura M, Kumakura T, Shiozaki K, Nakajima Y (1997) In: Stimming U, Singhal SC, Tagawa H, Lehnert W (eds) SOFC-V. The Electrochemical Society, Inc., Pennington, p 549
217. Lai TS, Barnett SA (2007) J Power Sources 164:742. doi:10.1016/j.jpowsour.2006.10.075
218. Jiang SP (2003) J Mater Sci 38:3775. doi:10.1023/A:1025936317472
219. Iwata T (1996) J Electrochem Soc 143:1521. doi:10.1149/1.1836673
220. Simwonis D, Tietz F, Stover D (2000) Solid State Ionics 132:241. doi:10.1016/S0167-2738(00)00650-0
221. Itoh H, Yamamoto T, Mori M, Horita T, Sakai N, Yokokawa H et al (1997) J Electrochem Soc 144:641. doi:10.1149/1.1837460
222. van Roosmalen JAM, Cordfunke EHP, Huijsmans JPP (1993) Solid State Ionics 66:285. doi:10.1016/0167-2738(93)90418-3
223. Stevenson JW, Hallman PF, Armstrong TR, Chick LA (1995) J Am Ceram Soc 78:507. doi:10.1111/j.1151-2916.1995.tb08207.x

224. Katayama K, Ishihara T, Ohta H, Takeuchi SJ, Esaki Y, Inukai E (1989) Nippon Seramikkusu Kyokai Gakujutsu Ronbunshi—J Ceram Soc Jpn 97:1327
225. Poirson A, Decorse P, Caboche G, Dufour LC (1997) Solid State Ionics 99:287. doi:10.1016/S0167-2738(97)00260-9
226. Mori M (2005) J Electrochem Soc 152:A732. doi:10.1149/1.1864312
227. Jorgensen MJ, Holtappels P, Appel CC (2000) J Appl Electrochem 30:411. doi:10.1023/A:1003987318963
228. Jiang SP, Wang W (2005) Solid State Ionics 176:1185. doi:10.1016/j.ssi.2005.02.013
229. Badwal S, Foger K (1998) In: Stevens P (ed) Third European SOFC forum. The European Fuel Cells Group, Lucerne, p 95
230. Tietz F (2004) In: Morgensen M (ed) Sixth European SOFC forum. The European Fuel Cells Group, Lucerne, p 289
231. Singhal SC (1997) In: Stimming U, Singhal SC, Tagawa H, Lehnert W (eds) SOFC-V. The Electrochemical Society, Inc., Pennington, p 37
232. Kusnezoff M, Trofimenko N, Mosch S, Beckert W, Graff A, Altmann F (2007) ECS Trans 7:1033. doi:10.1149/1.2729199
233. Weber A, Manner R, Jobst B, Schiele M, Cerva H, Waser R et al (1996) In: Poulson FW, Bonanos N, Linderoth S, Mogensen M, Zacharau-Christiansen B (eds) Seventeenth Riso international symposium on materials science: high temperature electrochemistry: ceramics and metals. Riso National Laboratory, Roskilde, p 473
234. Sholklapper TZ, Radmilovic V, Jacobson CP, Visco SJ, De Jonghe LC (2007) Electrochem Solid-State Lett 10:B74. doi:10.1149/1.2434203
235. Herbstritt D, Weber A, Ivers-Tiffee E (1999) In: Singhal SC, Dokiya M (eds) SOFC-VI. The Electrochemical Society, Inc., Honolulu, p 972
236. Bergsmark E, Furuseth S, Dyrlie O, Norby T, Kofstad P (1991) In: Grosz F, Zegers P, Singhal SC, Yamamoto O (eds) SOFC-II. Commission of the European Communities, Luxembourg, p 473
237. Liang FL, Chen J, Cheng JL, Jiang SP, He TM, Pu J et al (2008) Electrochem Commun 10:42. doi:10.1016/j.elecom.2007.10.016
238. Ralph JM, Schoeler AC, Krumpelt M (2001) J Mater Sci 36:1161. doi:10.1023/A:1004881825710